

What is global seismic tomography?

- Whole mantle from large, consistent datasets.
- Context for regional studies

Karaisan < van der Kist (ISC)

112

CHAPTER 4. MANTLE P-WAVE SPEED

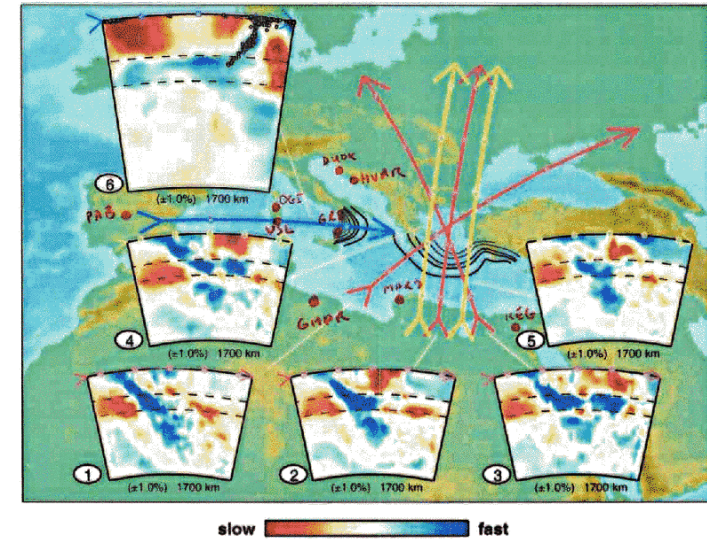


Figure 4-8: Cross sections through active subduction zones around the Mediterranean. Gray scale contours show outlines of subduction zones from Gudmundsson and Sambridge [1998]. Location of cross sections is indicated and circular markers are placed 5° apart. Limits of the color-scale and the depth extent are indicated at the bottom of each section.

could be related to closing/reopening events of the Tethys sea, as it seems connected to the much larger anomaly around mid-mantle depths along the southern margin of Asia as seen in Figure 4-5d-e. For cross sections 1 through 5, the inversion tests (Figure 4-11) suggest excellent resolution and indicate that, for instance, the apparent disconnection between the lower and upper mantle structures is real. Cross section 6 shows subduction in southern Italy and across the Tyrrhenian sea. The resolution is worse, but horizontal smearing in the

Some General Issues

What determines the nature of the final model?

- Data (single data type/mixed data types) (very important – e.g. upper mantle of ISC-only models will be incomplete at best)
- Parameterization (blocks/ spherical harmonics/ etc.) (not important except from a practical point of view)
- Inversion technique (iterative/direct) (not important except from a practical point of view)

(BUT.... details are very important – crust corrections, location errors, ...) *← source*

AND... what about anisotropy?

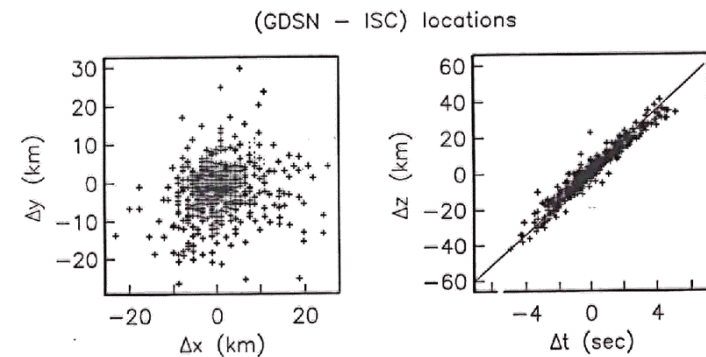
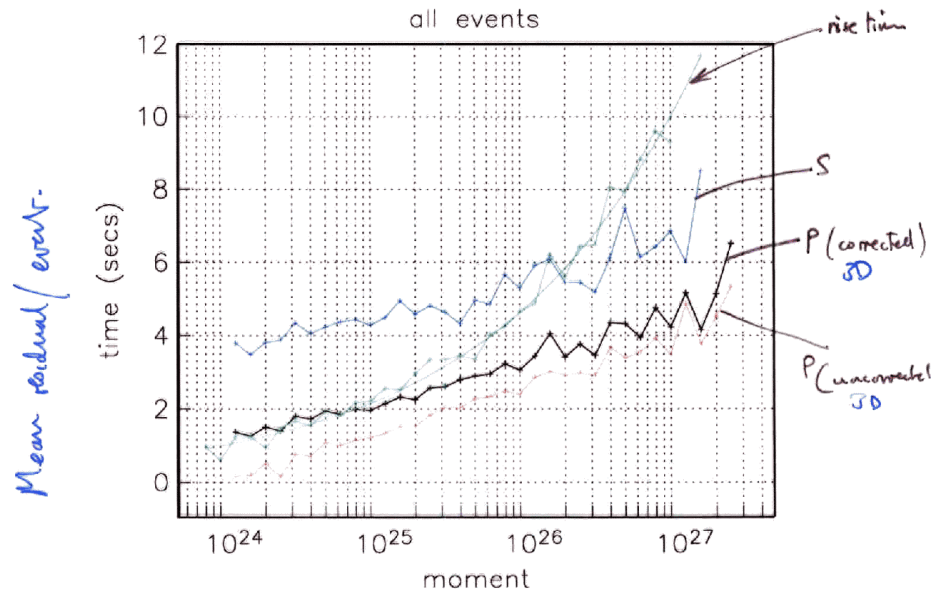


Figure 9. An analysis of the differences between the PDE locations and the ISC locations. Left: the scatter reflecting differences in longitude and latitude – there is no correlation. Right: the scatter in differences between origin time and event depth – note the almost perfect correlation.



$$M_0 = \mu A d$$

moment area of fault average slip

L = length of fault

Constant stress drop $\Rightarrow d \propto L$

$$A \propto L^2$$

$$\therefore M_0 \propto L^3$$

$$t_{rise} = \frac{L}{V_r} \quad \therefore M_0 \propto t_{rise}^3$$

$$t_{rise} \propto M_0^{1/3}$$



Handling mislocation

$$\underline{\delta t} = \underline{A} \underline{\delta h} + \underline{B} \underline{\delta v}$$

①

Projection

$$\underline{P} \underline{A} = 0$$

$$\text{if } \underline{A} = \underline{U} \underline{\Lambda} \underline{V}^T \quad (\text{SVD})$$

$$\underline{P} = \underline{G} (\underline{I} - \underline{U} \underline{U}^T)$$

(G chosen to make new data independent)

$$\underline{P} \underline{\delta t} = \underline{P} \underline{A} \underline{\delta h} + \underline{P} \underline{B} \underline{\delta v} = \underline{P} \underline{B} \underline{\delta v} \quad *$$

②

Relocation

$$\underline{\delta t} = \underline{A} \underline{\delta h}$$

$$\underline{\hat{\delta h}} = \underline{A}^{-1} \underline{\delta t} = \underline{V} \underline{\Lambda}^{-1} \underline{U}^T \underline{\delta t}$$

$$\underline{\delta t} - \underline{A} \underline{\hat{\delta h}} = (\underline{I} - \underline{U} \underline{U}^T) \underline{\delta t} = \underline{B} \underline{\delta v} \quad *$$

Similar but different!

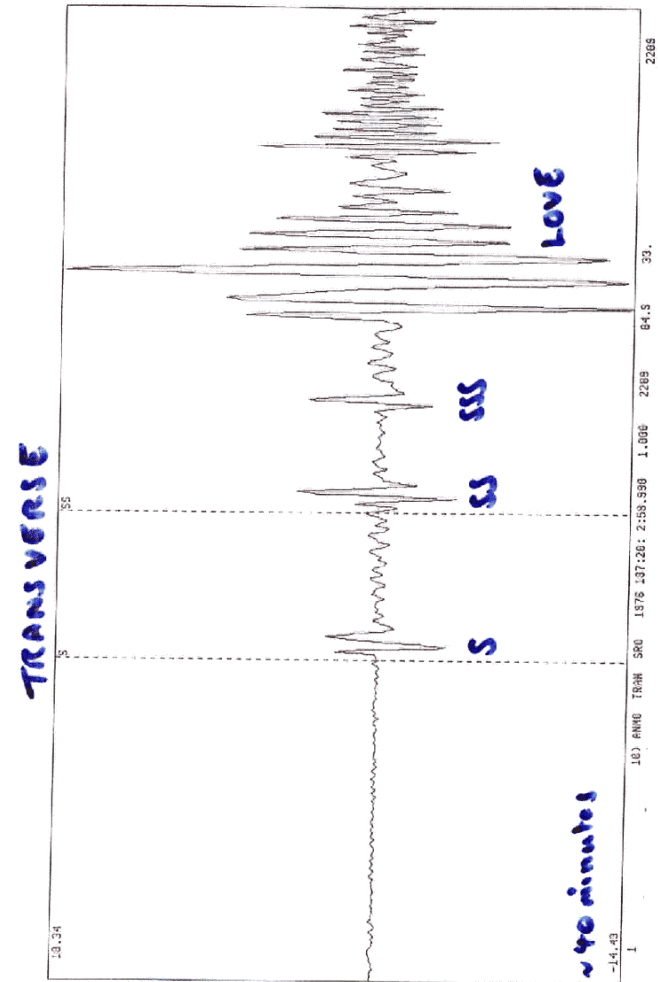
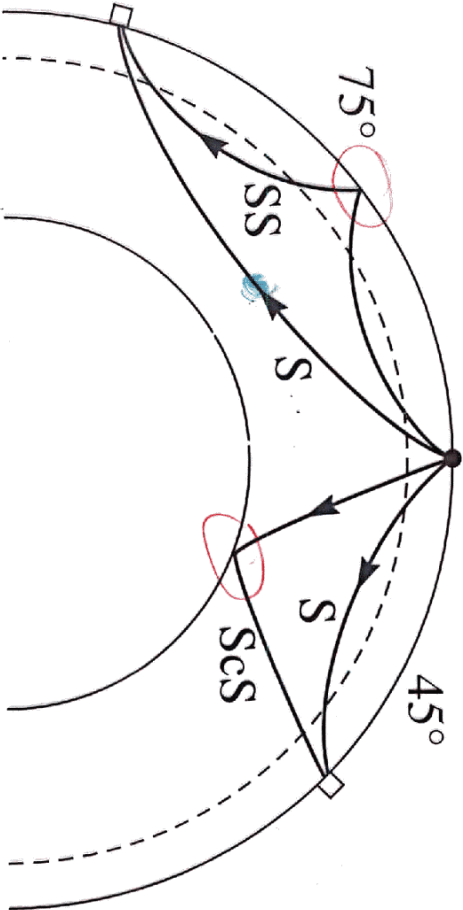
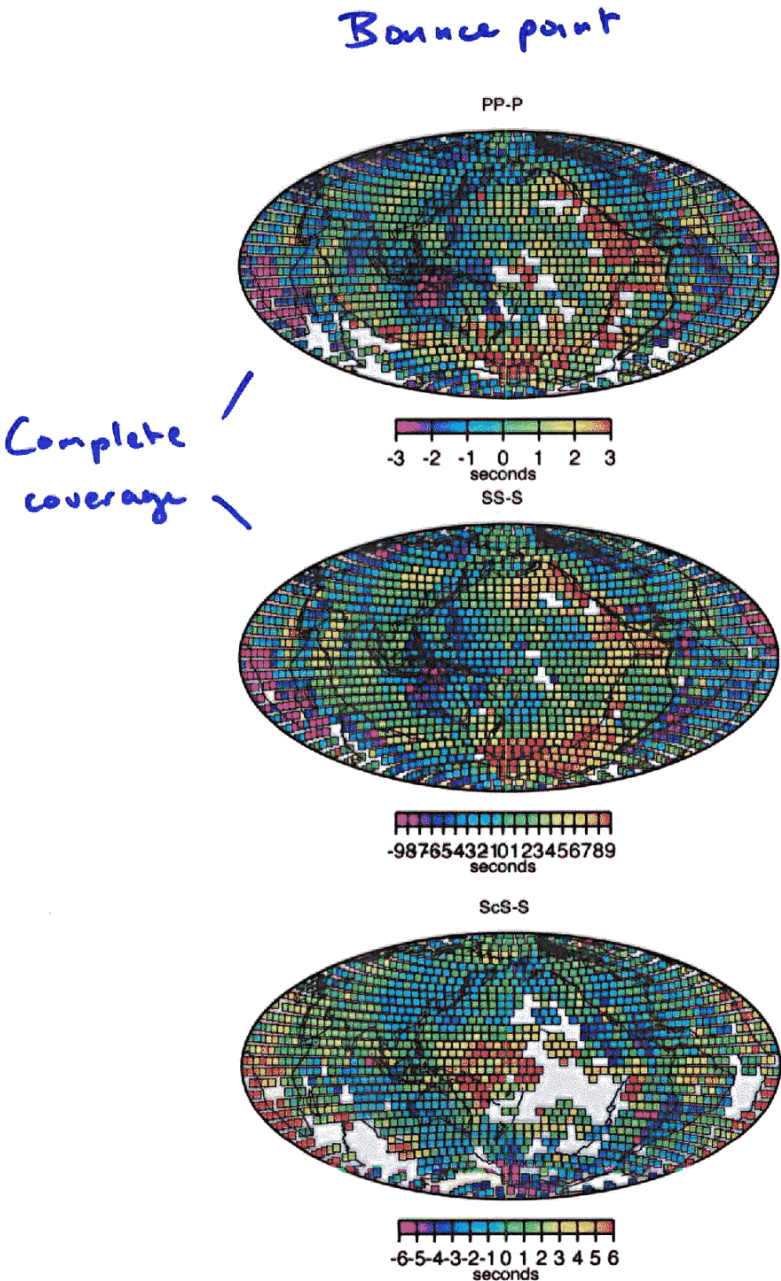


Figure 7. A transverse component seismogram recorded at station ANMO at an epicentral distance of 84.9°. Note the clear SSS arrival and the onset of SSSS leading into the Love wave. These phases are useful for improving depth resolution on upper mantle structure.



SS-S and ScS-S Ray Path Geometries



$$T = \int \frac{1}{v} d\Gamma$$

$$\delta T = - \int \frac{1}{v^2} \delta v d\Gamma$$

Suppose δv is concentrated on the ray somewhere (P & S rays are very similar)



$$\delta T_S = - \frac{1}{v_S} \frac{\delta v_S}{v_S} X$$

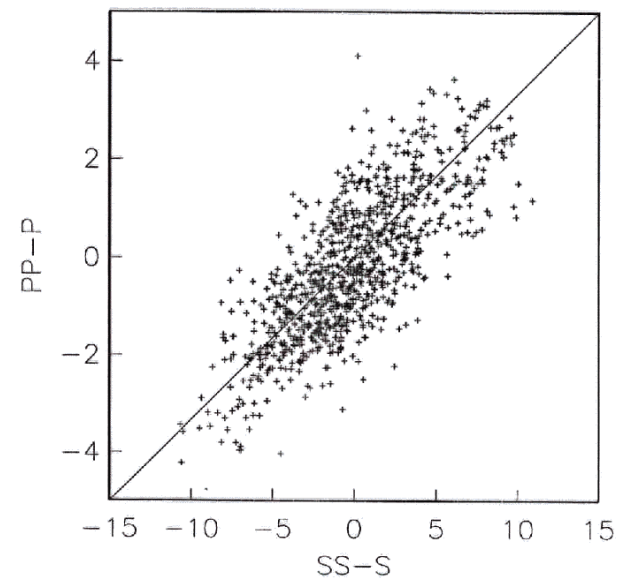
$$\delta T_P = - \frac{1}{v_P} \frac{\delta v_P}{v_P} X$$

$$\therefore R = \frac{\partial \ln v_S}{\partial \ln v_P} \approx \frac{v_S}{v_P} \frac{\delta T_S}{\delta T_P}$$

$\sqrt{\frac{1}{5}}$

$$\delta T_{SS-S} \approx 3 \delta T_{PP-P}$$

$$\Rightarrow \frac{\partial \ln v_S}{\partial \ln v_P} \approx 1.7$$



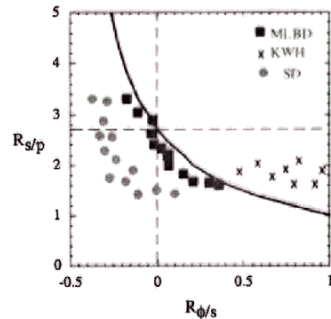


Figure 1. Relation between R_{SD} and R_{KH} for $A=0.37$. The solid curve shows a theoretical relation for equation (13). $R_{SD} = 1$ when $R_{KH} = 0$ and $R_{SD} \rightarrow \infty$ as $R_{KH} \rightarrow A/(1-A)$. Seismological models are also shown. MLBD, Masters *et al.* [2000]; SD, Su and Dziewonski [1997]; KWH, Kennett *et al.* [1998]. Data points for MLBD and SD are the mean values of these ratios whereas those for KWH are the root-mean square values of these ratios. The results of Masters *et al.* [2000] are in good agreement with the relation (13), but neither the results by Su and Dziewonski [1997] nor by Kennett *et al.* [1998] is consistent with the relation (13). Su and Dziewonski [1997] inferred largely negative values of R_{SD} (<-0.2) in most of the lower mantle which would imply very large R_{KH} exceeding -4 , which is inconsistent with their observation of $R_{KH} = 1.5$ –3.1. Similarly Kennett *et al.* [1998] obtained negative values of R_{SD} in the deep lower mantle where they obtained $R_{KH} = 2$ which is inconsistent with (13). They only showed root-mean-square values of R_{SD} , which are always positive. Therefore their data on R_{SD} and R_{KH} from deep lower mantle are not shown in this diagram.

where $\alpha_m = (-\log \rho \theta')$, is the coefficient of thermal expansion. The temperature effects on elastic moduli may come from anharmonic effects and aelastic effects. Anharmonicity refers to the behavior of materials in which elastic properties change because of temperature (or pressure) caused by the deviation of lattice vibration from harmonic oscillator [e.g., Anderson, 1995]. This does not involve any energy dissipation. One of the main consequences of anharmonicity is thermal expansion, and elastic properties of materials can change due to the change in mean atomic distances. Therefore anharmonicity involves a large change in density and hence results in large values of R_{slip} .

Another important process whereby seismic wave velocities may vary is anelasticity. This is a dissipative process involving some viscous deformation [e.g., *Karato and Spetzler, 1990; Jackson, 2000*]. The degree to which viscous deformation affects seismic wave velocities is measured by Q factor and depends on the frequency of seismic waves. Consequently, anelasticity results in the frequency dependence of seismic wave velocities. The importance of anelasticity in the interpretation of seismological models at different frequencies was recognized in the mid 1970s [e.g., *Kanamori and Anderson, 1977*], and its significance in interpreting seismic tomography was first recognized by *Karato* [1993]. Because changes in seismic wave velocities caused by enhanced anelasticity are not associated with significant volume change, the density to velocity anomaly ratios ($R_{\rho v}$) tend to be small when anelasticity plays an important role. Also, contributions from anelasticity significantly increase the absolute values of temperature derivatives of shear wave velocities but not bulk sound wave velocities, resulting in an increase in R_{Kp} .

Most of the usual laboratory measurements of temperature dependence of elasticity are made at ultrasonic frequencies (~1 MHz to ~1 GHz) [e.g., Anderson *et al.*, 1992; Anderson, 1995; Sinelnikov *et al.*, 1998]. At these frequencies, anelastic relaxation is negligible and therefore these measurements provide us with a measure of the effects of anharmonicity. Parameters corresponding to anharmonicity are referred to Anderson-

Table 1. Anharmonic Parameters and Velocity Heterogeneity Ratio, R_{sp} , for Mantle Minerals*

	δ_S	Γ	R_{SP}	α_a ($10^{-5} K^{-1}$)
NaCl	4.02	6.10	1.13	11.8
MgO	3.12	5.05	1.31	3.1
CaO	3.58	4.94	1.22	2.9
Grossular	3.29	4.96	1.29	2.0
Pyrope	3.97	4.10	1.06	2.0
Olivine (Fo90)	4.14	5.35	1.18	2.5
Olivine (Fo100)	4.05	5.44	1.22	2.5
Co ₂ SiO ₄	4.88	4.62	0.96	
MgAl ₂ O ₄	4.74	4.11	0.90	2.1
Al ₂ O ₃	3.55	6.11	1.36	2.3
Wadsleyite ^b	4.7	6.4	1.20	2.1
Ringwoodite ^b	4.7	6.5	1.21	2.0
MgSiO ₃ perovskite	4.0 ^b	5.7 ^b	1.14 ^b	3.0 ^b
	3.4 ^c	5.4 ^c	1.44 ^c	3.0 ^c

^a Data from Anderson [1989] unless otherwise noted.

^b Data are calculated from systematics (Anderson [1989]).

^c Data from *Funamori et al.* [1996] and *Sinel'nikov et al.* [1998] at ~8 GPa.

Temperature dependence of velocities

For a frequency-independent Q , the seismic velocity depends on frequency and temperature (T) as

$$v(\omega, T) = v_0(T) \left[1 + \frac{1}{\pi Q} \ln(\omega \tau) \right]$$

v_0 corresponds to the unrelaxed velocity, and the relaxation time, τ , is of the form

$$\tau(T) = \tau_0 \exp (H^* / R_g T)$$

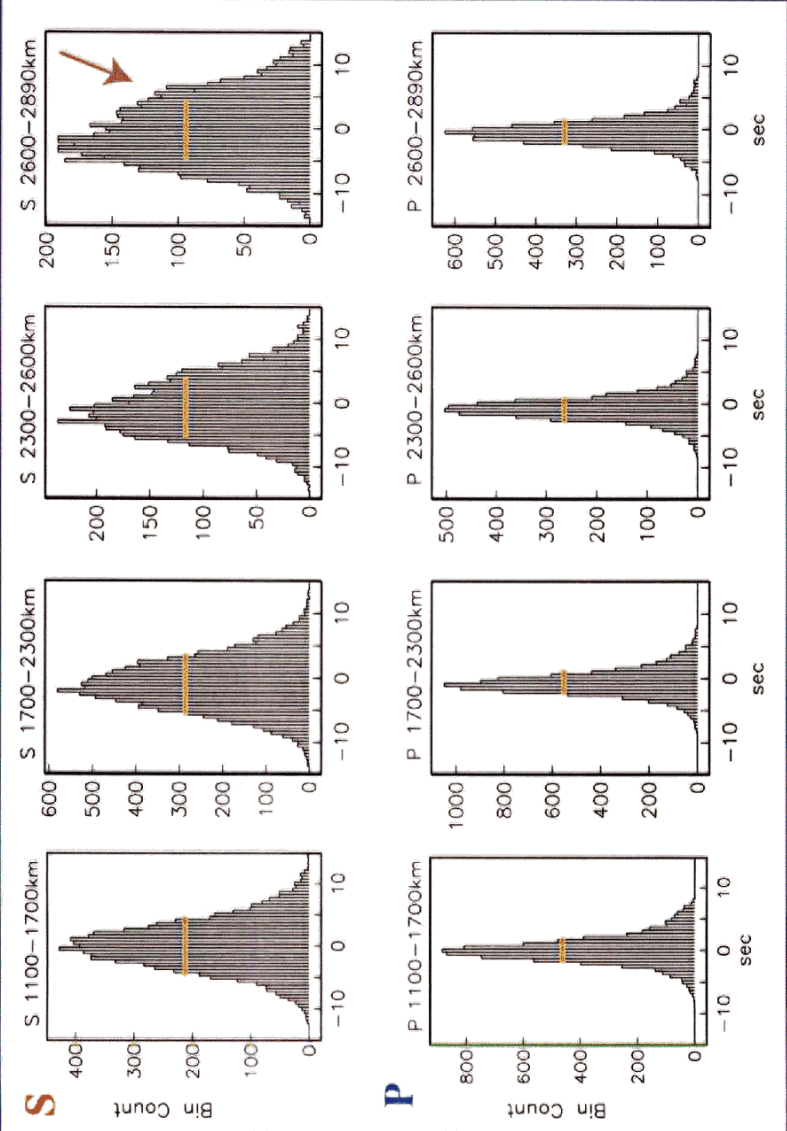
H^* is the activation enthalpy, R_g is the gas constant. Differentiating with respect to temperature gives

$$\frac{\partial \ln v}{\partial T} = \frac{\partial \ln v_0}{\partial T} - \frac{1}{\pi Q} \frac{H^*}{R_g T^2}$$

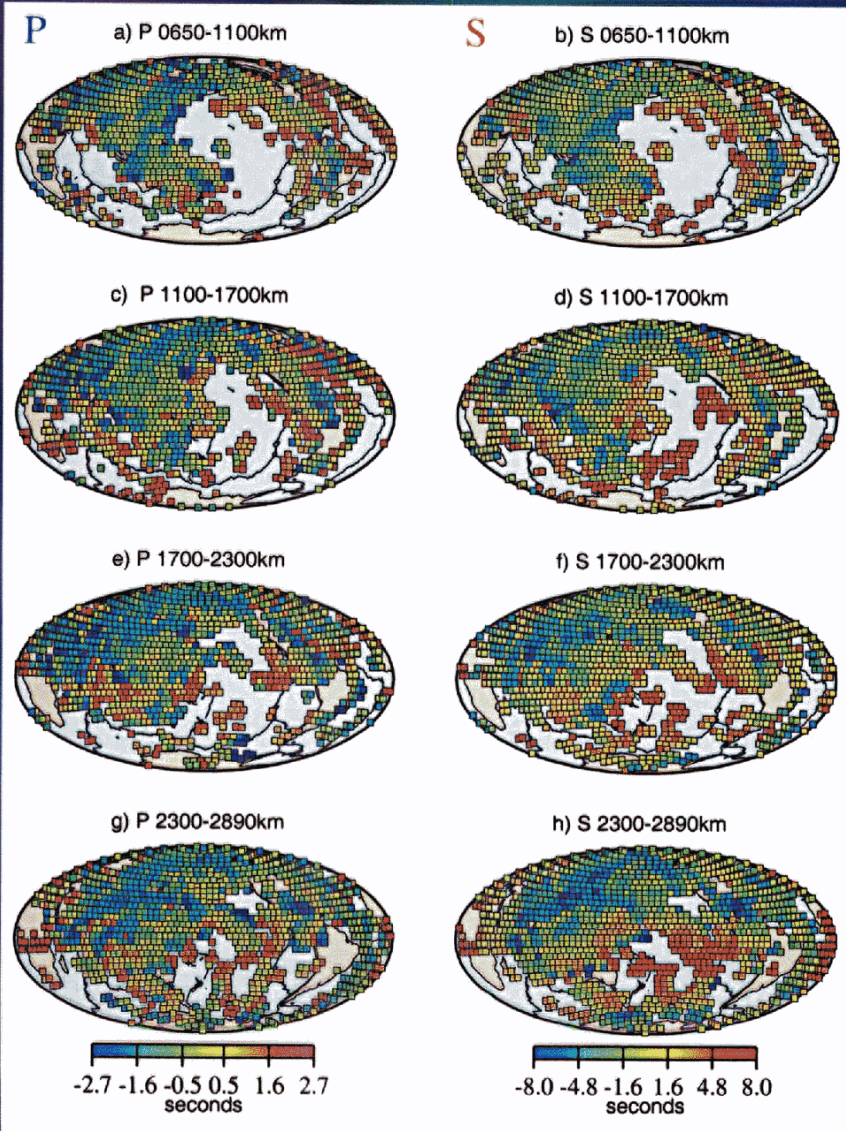
anharmonic

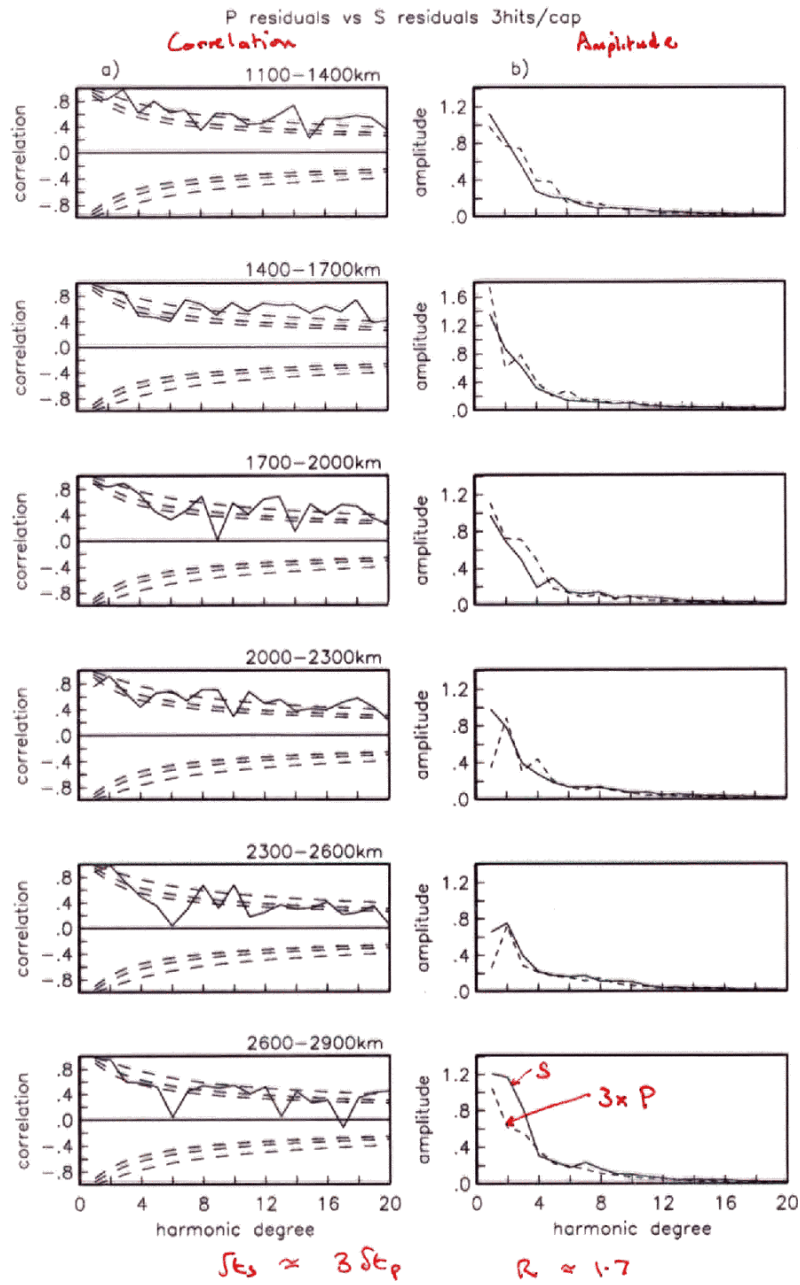
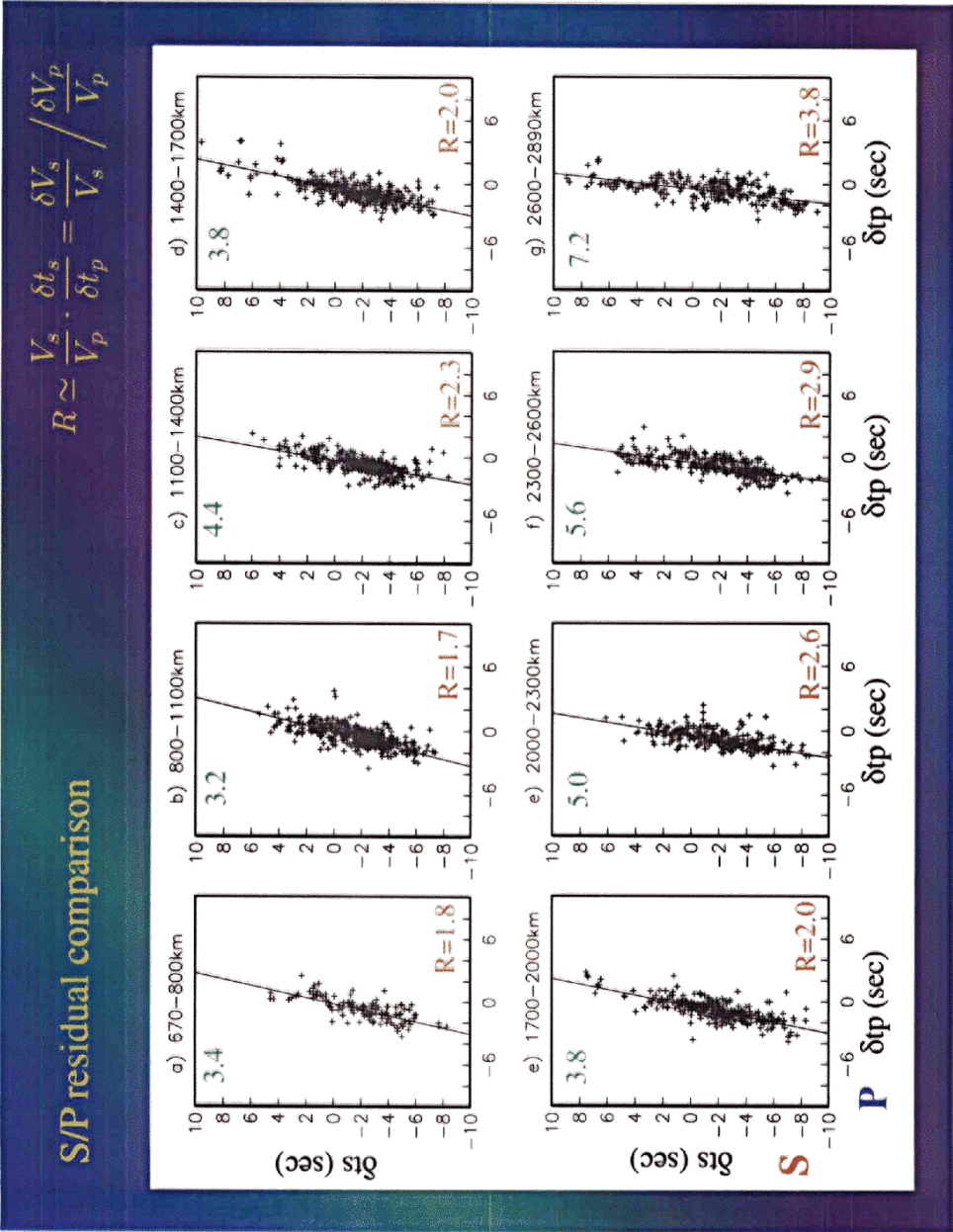
anelastic
(unimportant for V_c)

S and P residuals sorted by ray turning depth

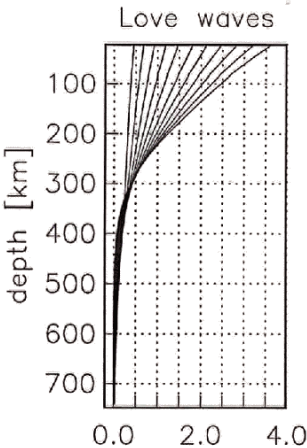
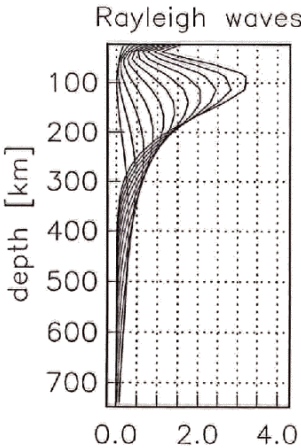
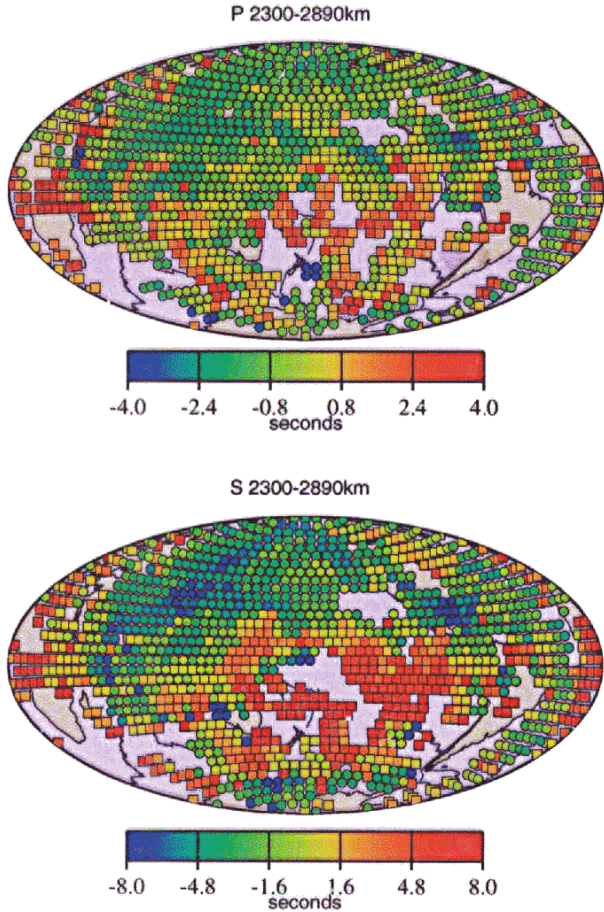


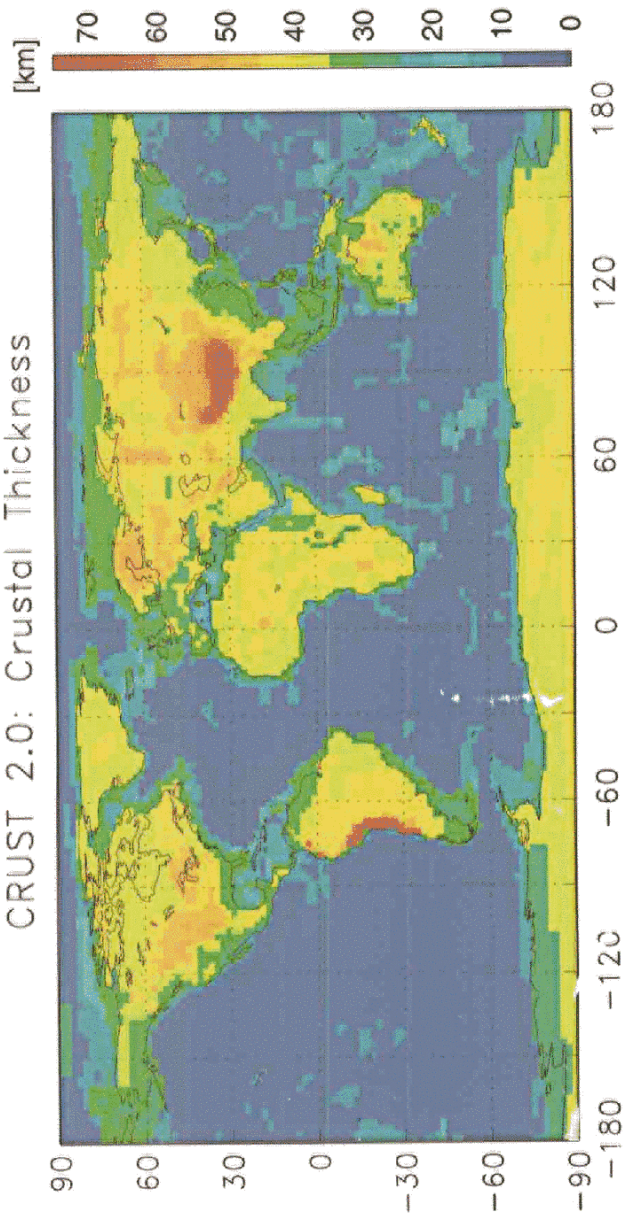
P and S residuals sorted by ray turning depth



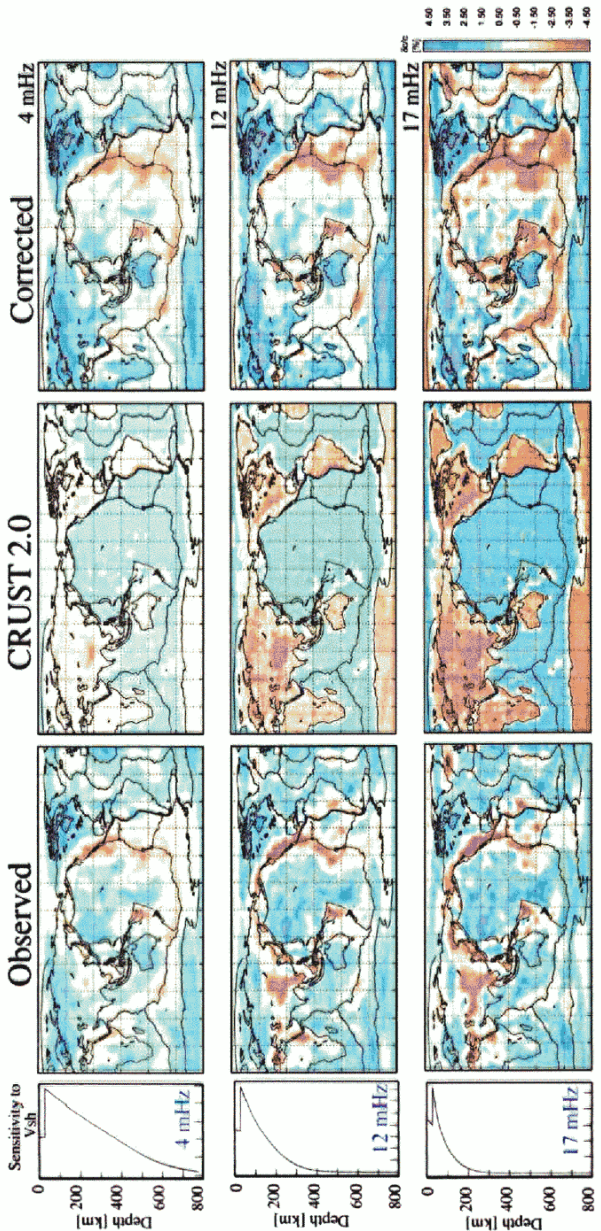


P & S turning in lowermost mantle
- residuals binned at turning point





The Effects of Crustal Correction on Love Wave Phase Velocity



Parameterization

- Global bases (e.g. spherical harmonics) have been used in conjunction with a layer, polynomial (Chebyshev, Legendre), or B-spline parameterization radially. Global bases are nice for data which naturally average over large distances (mode structure coefficients, long period dispersion data).
- Global bases are impractical for use with large body-wave datasets where it is important to take advantage of sparsity
- Local bases typically are blocks, spherical B-splines, tessellations, etc. More sophisticated analyses vary block size to reflect ray sampling
- Some recent inversions take account of finite frequency (non-ray) effects

Karason

106

CHAPTER 4. MANTLE P-WAVE SPEED

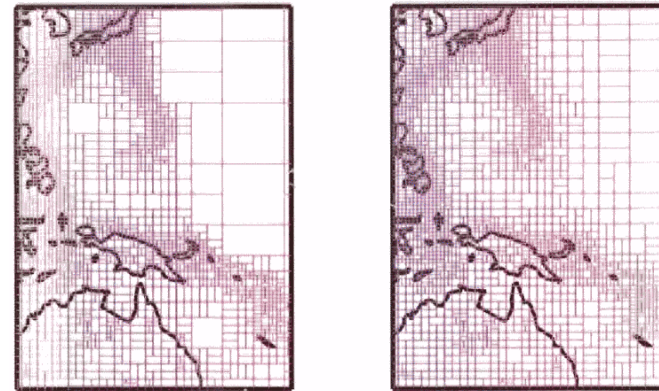


Figure 4-4: (a) Adaptive grid before spatial smoothing is applied and (b) after.

4.4 Results

4.4.1 Global structure

Figure 4-5 depicts wave speed variations according to the model at selected depths in the mantle. From a global perspective, the results are consistent with our former studies using regular grids, i.e. *Karason and van der Hilst* [2001] and *van der Hilst et al.* [1997], and our analysis and interpretation of this part of the model will therefore be brief. Slow back are regions and fast subduction zones along with craton signatures are prominent at shallow depths. Deeper, the model is marked by long and narrow traces of fast material from the upper mantle transition zone to mid-mantle depths beneath North and South America and beneath southern Asia. These structures have been associated with plate motion history and are thought to be the remnants of old subducted slabs [*van der Hilst et al.*, 1997; *Grand*

good for ISC

Damping and the inversion

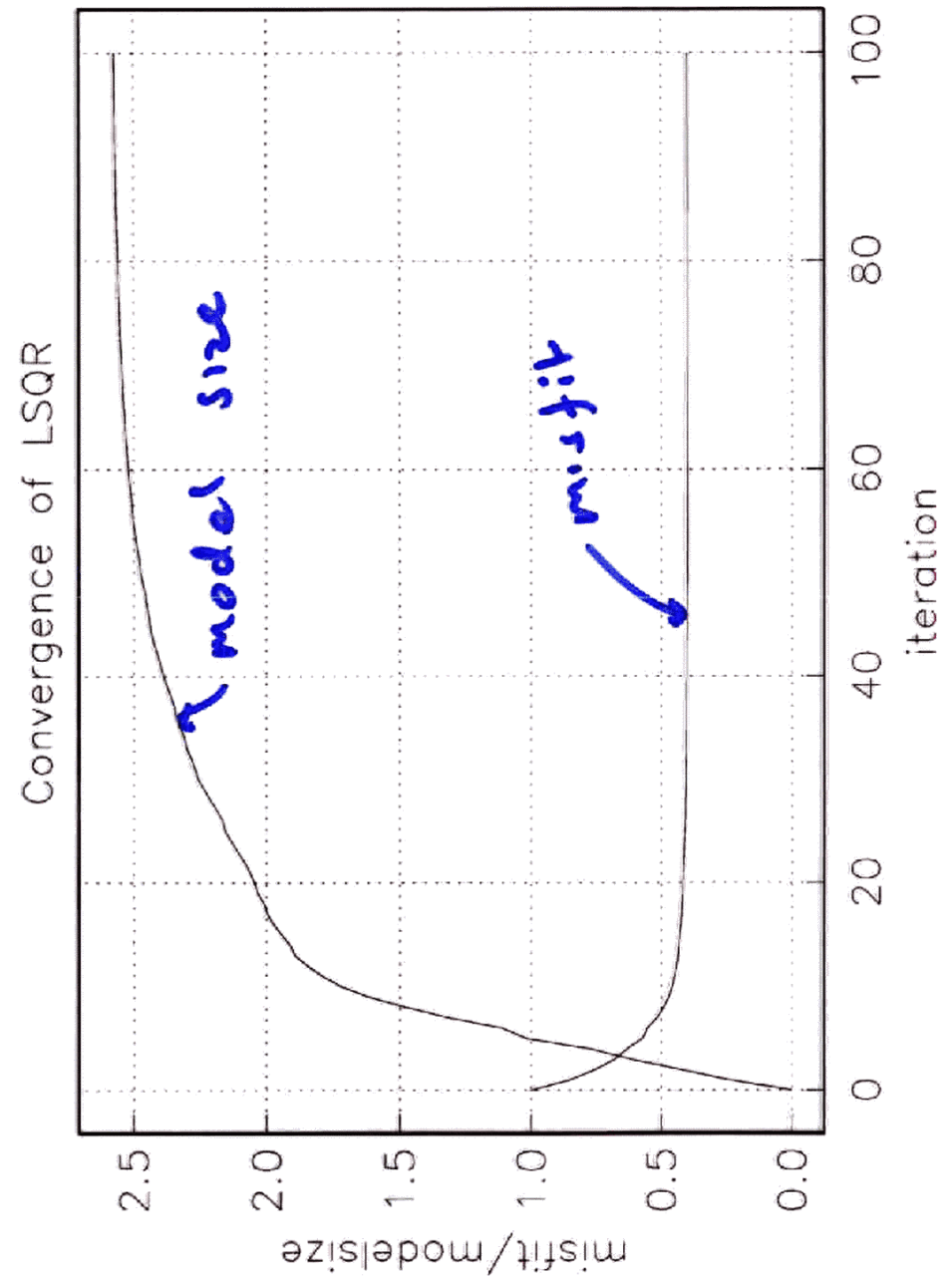
Minimize 2-norm plus some measure of roughness:

$$(\mathbf{A} \cdot \mathbf{x} - \mathbf{y})^2 + \lambda^2 (\mathbf{D} \cdot \mathbf{x})^2$$

D would be I for minimum norm damping (bad), or a first or second difference operator for gradient damping. We would typically have different λ 's for radial and lateral smoothing since the length-scales involved are very different.

Problem can be written in the usual form and solved by LSQR, SVD or anything else:

$$\begin{bmatrix} \mathbf{A} \\ \lambda \mathbf{D} \end{bmatrix} \cdot \mathbf{x} = \begin{bmatrix} \mathbf{y} \\ 0 \end{bmatrix}$$



An example S inversion

Data

- 28,000 SS-S data (distance range 48–100 degrees)
- 14,000 ScS-S data (distance range 44–78 degrees)
- 130,000 absolute S data (25–100 degrees)
- 29,000 absolute SS data (52 to 173 degrees)
- Love and Rayleigh wave dispersion data at 12 frequencies between 4 and 15 mHz

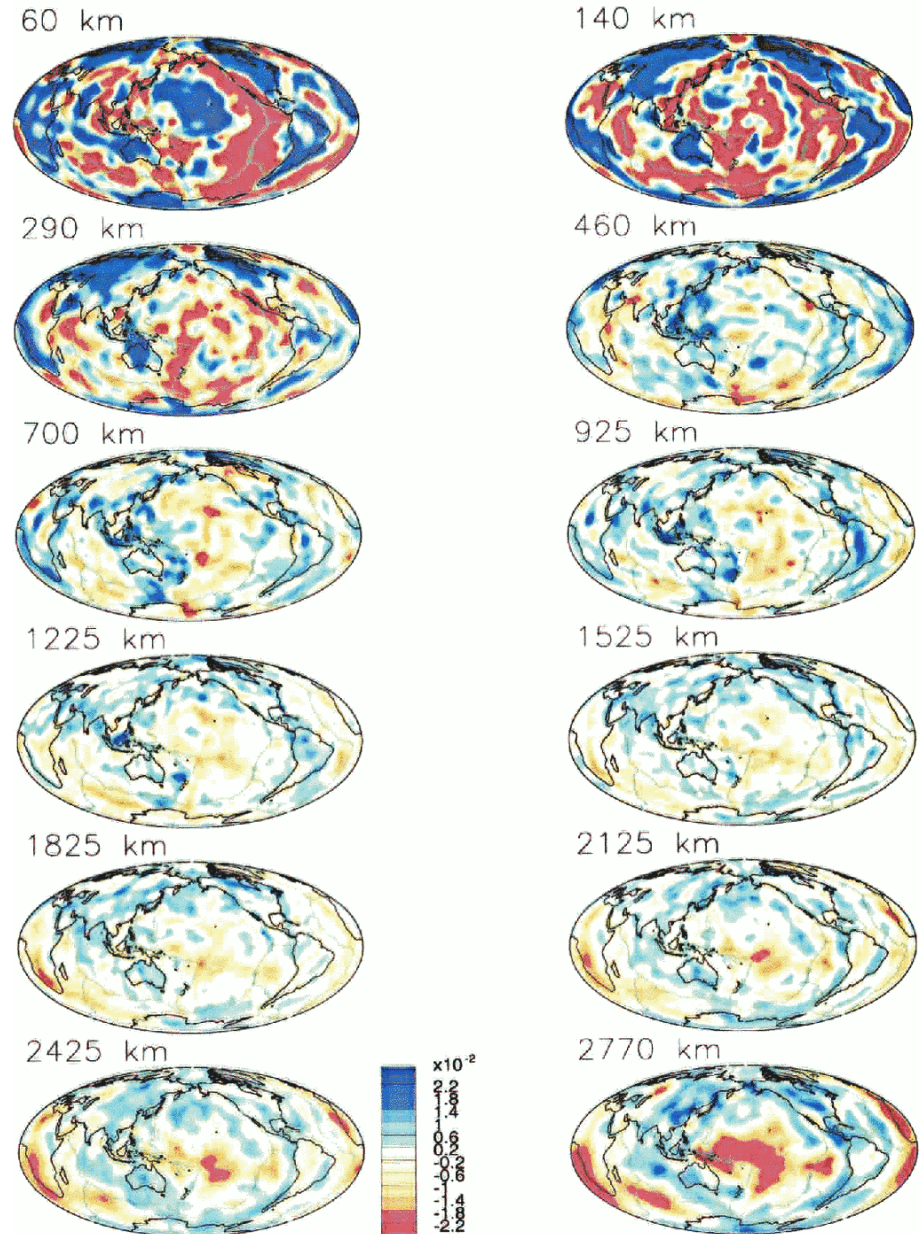
A total of up to 230,000 data

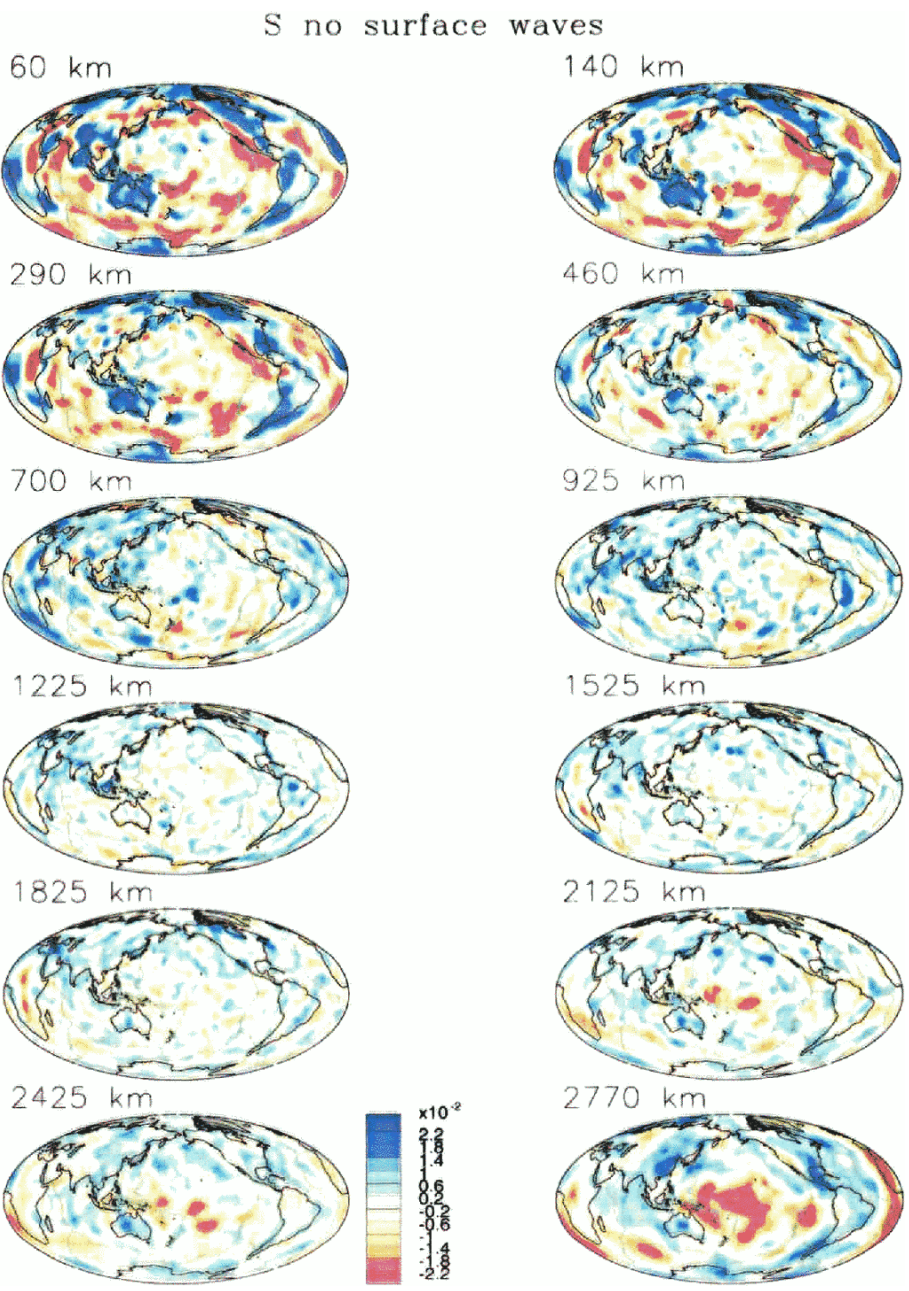
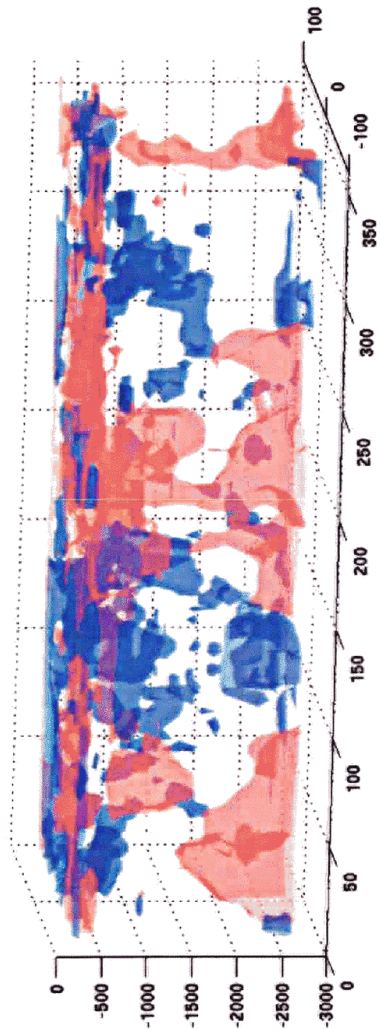
Parameterization

- Equal area blocks of dimension 4 degrees at the equator in 18 layers – layer thickness is on the order 100 km in the upper mantle and on the order of 200 km in the lower mantle.

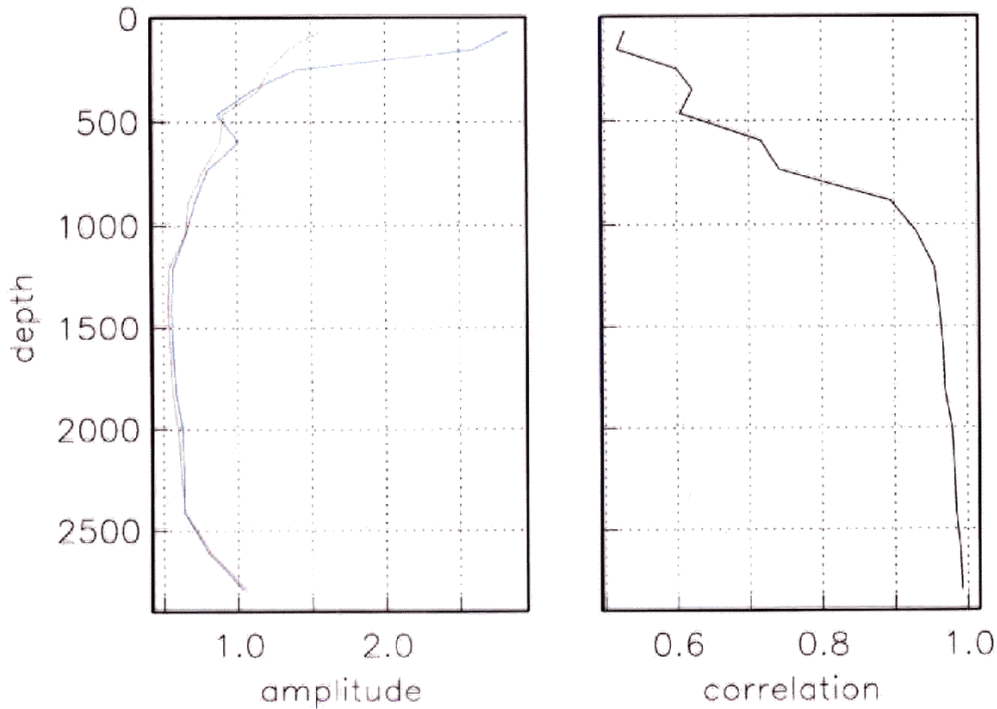
A total of 46,000 model parameters

S traditional data

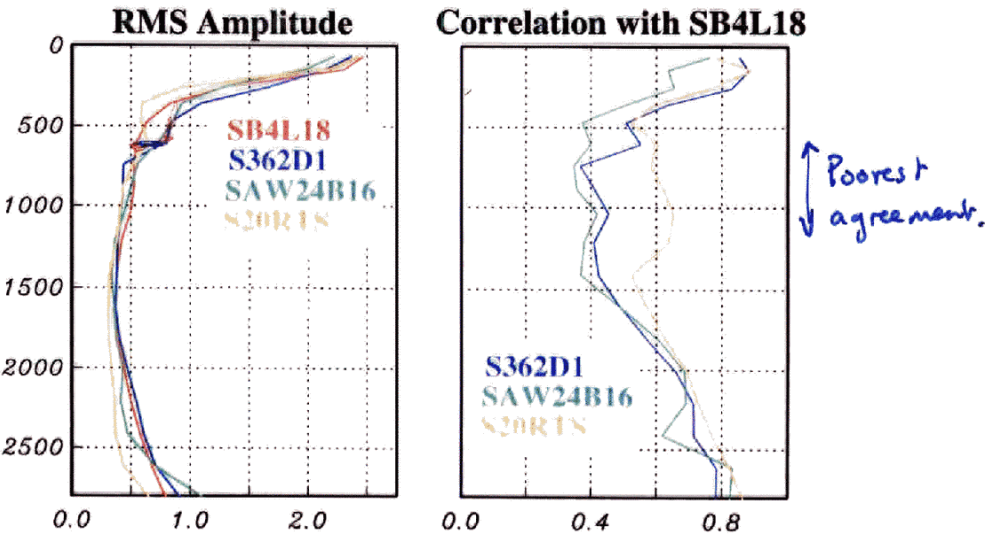




Effect of not having
surface waves



A Quantitative Comparison

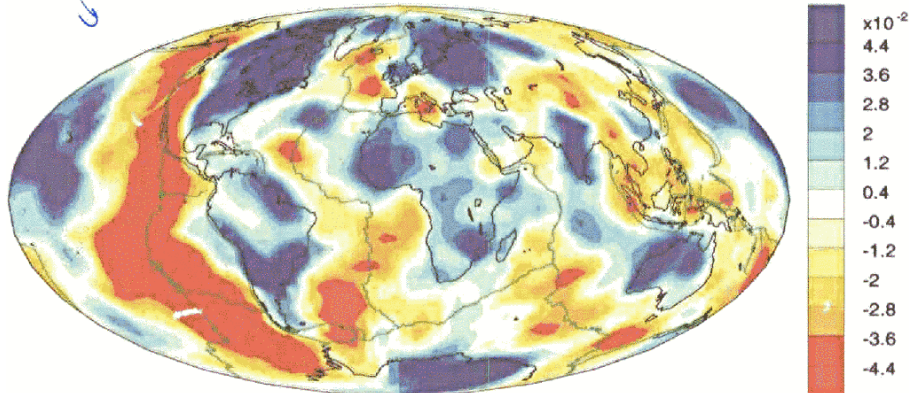


RMS Amplitudes and correlation between models
as function of depth

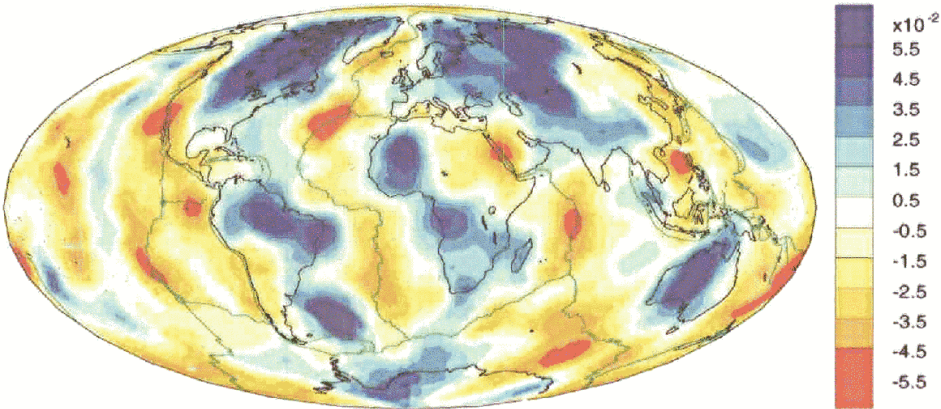
Large Anomalies

European projection

S below moho proj

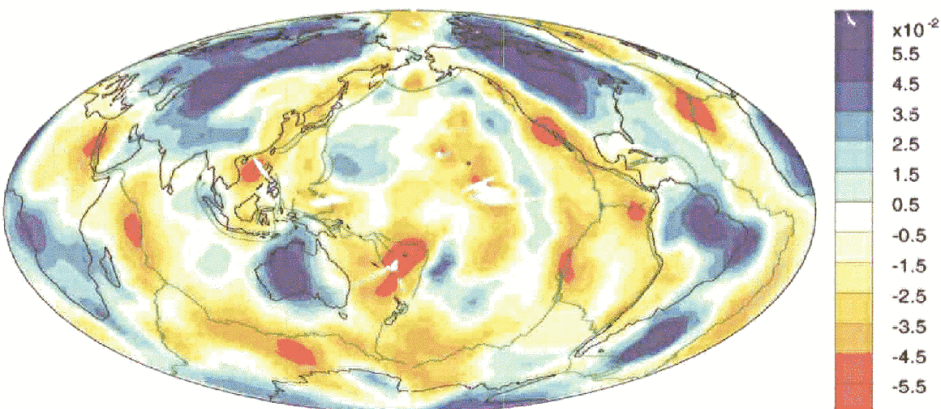
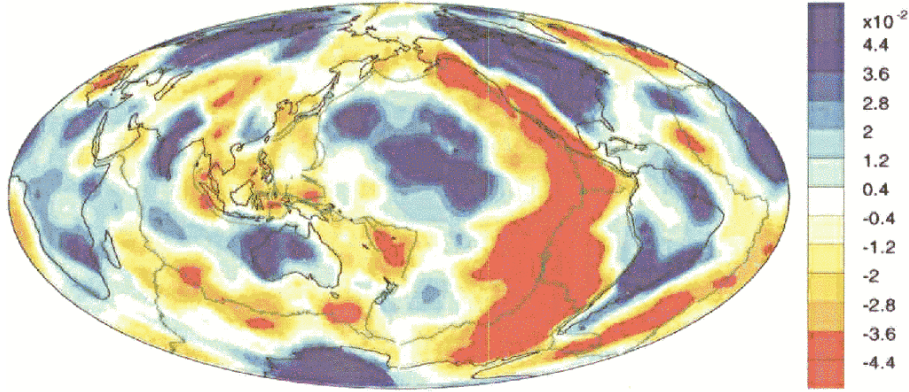


S at 150km proj



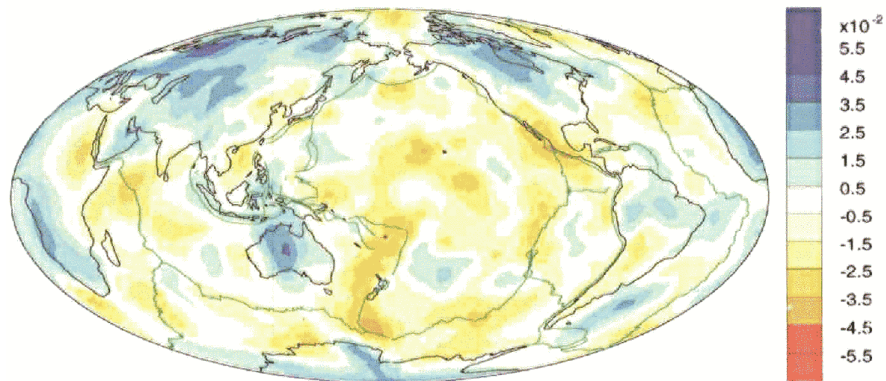
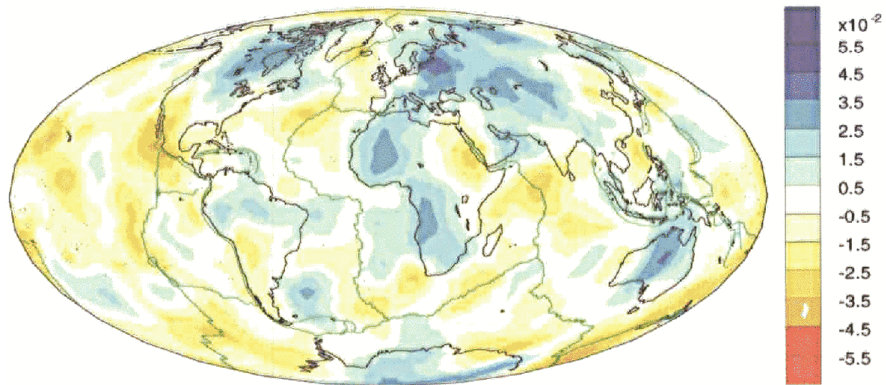
Still large
Don't see subduction zones?

USA projection



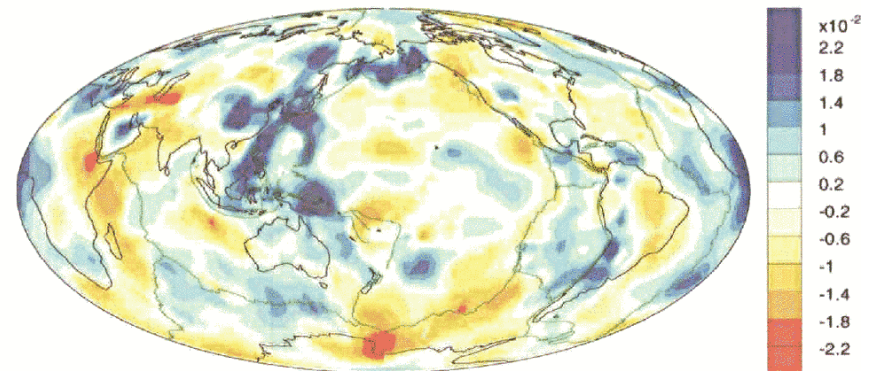
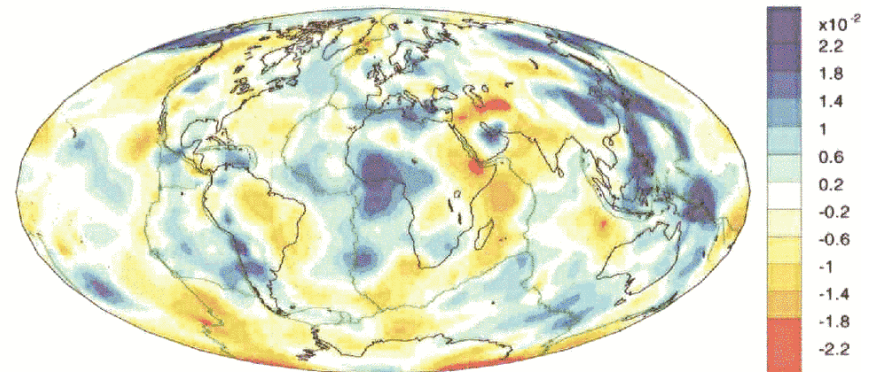
little of cratons left

S at 300km proj



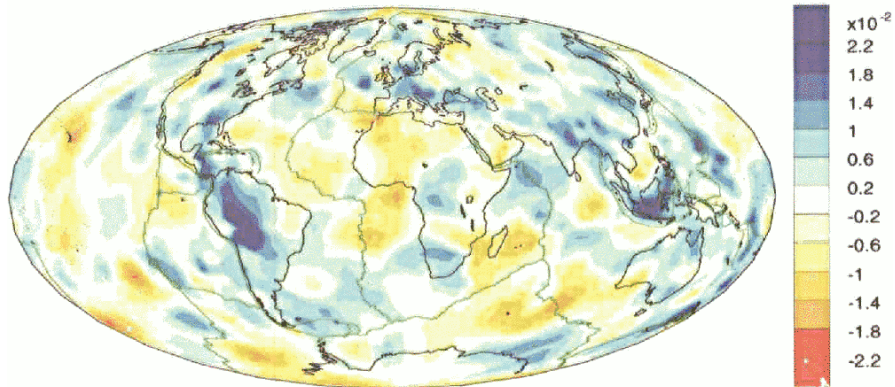
Scale change!
Subduction!

S in TZ proj

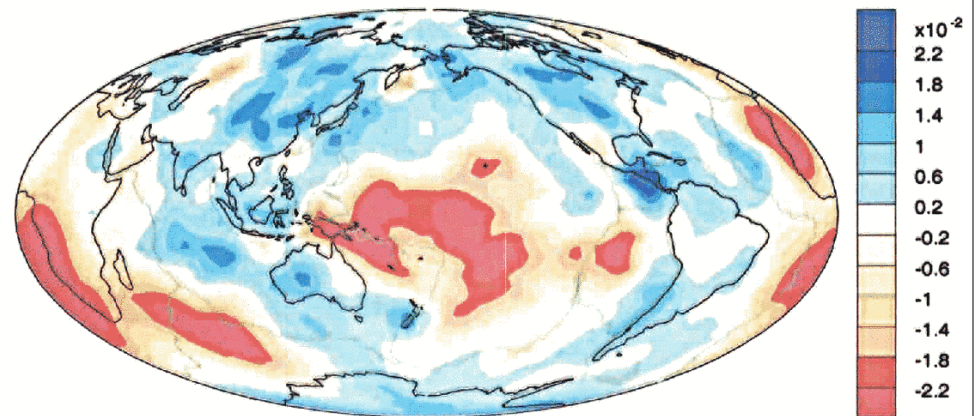
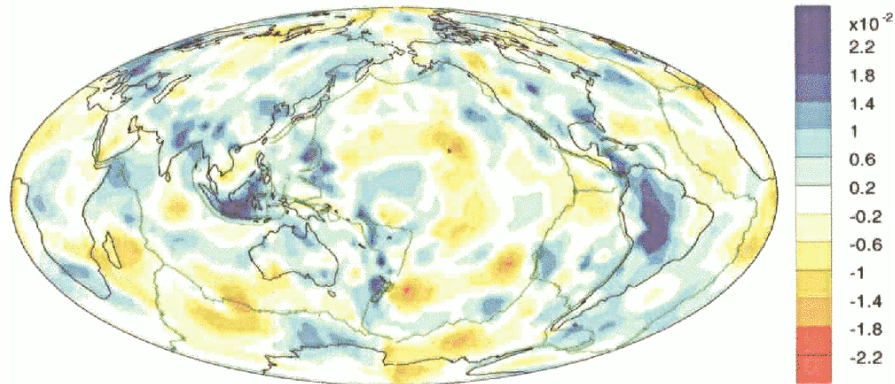
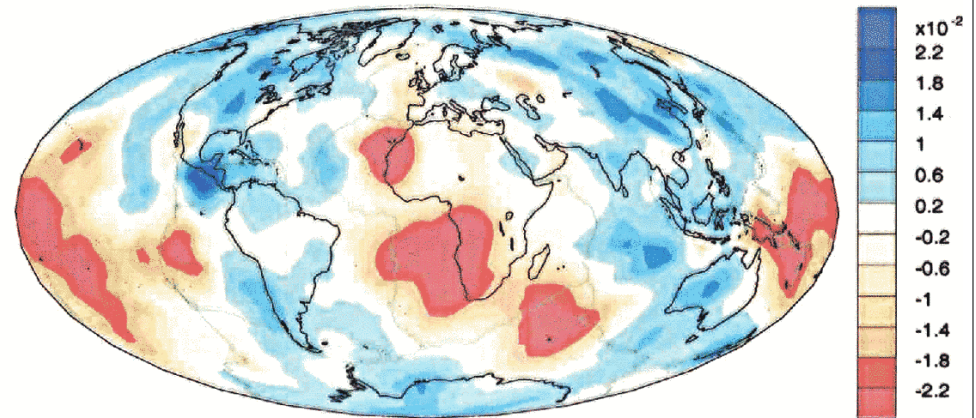


Possible slabs

S at 1000km

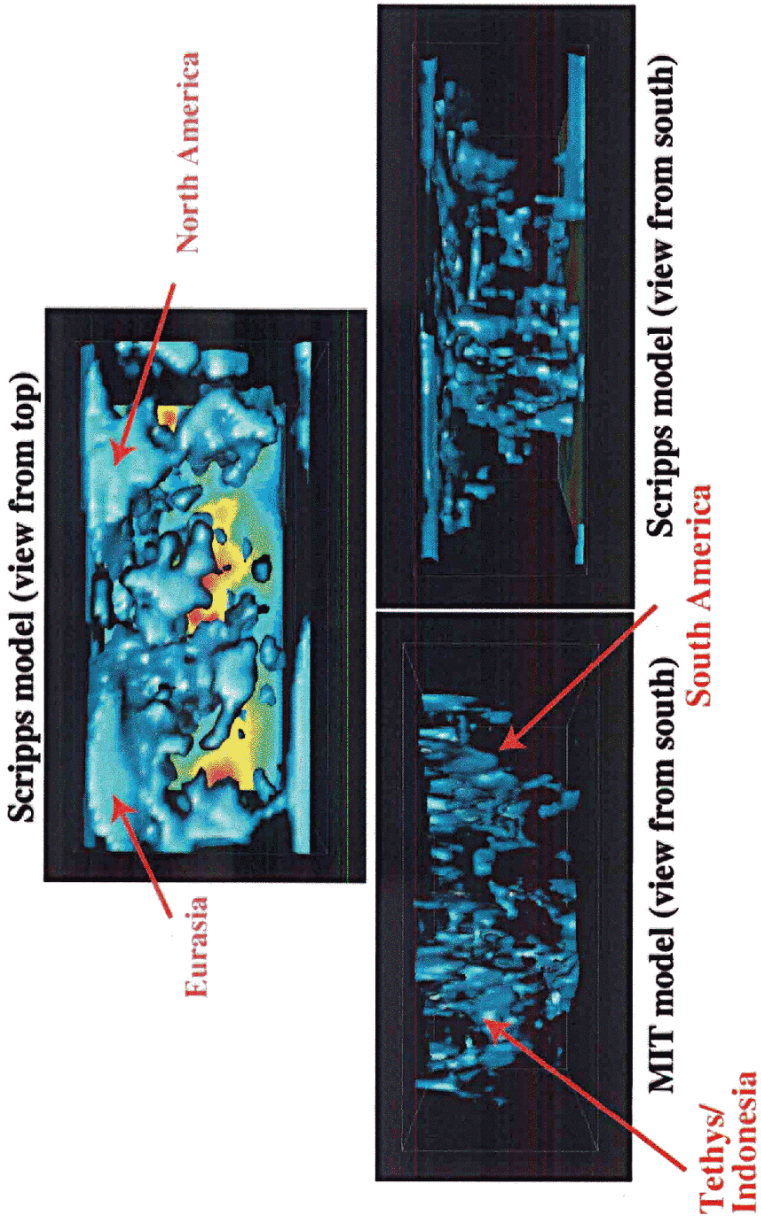


S at base of mantle



Plume groups?
Heat from core?

Subducting Slabs: Fading or Pervasive?



letters to nature

NATURE | VOL 397 | 21 JANUARY 1999 | www.nature.com

Mesozoic subducted slabs under Siberia

Rob Van der Voo*, Wim Spakman & Harmen Bijwaard

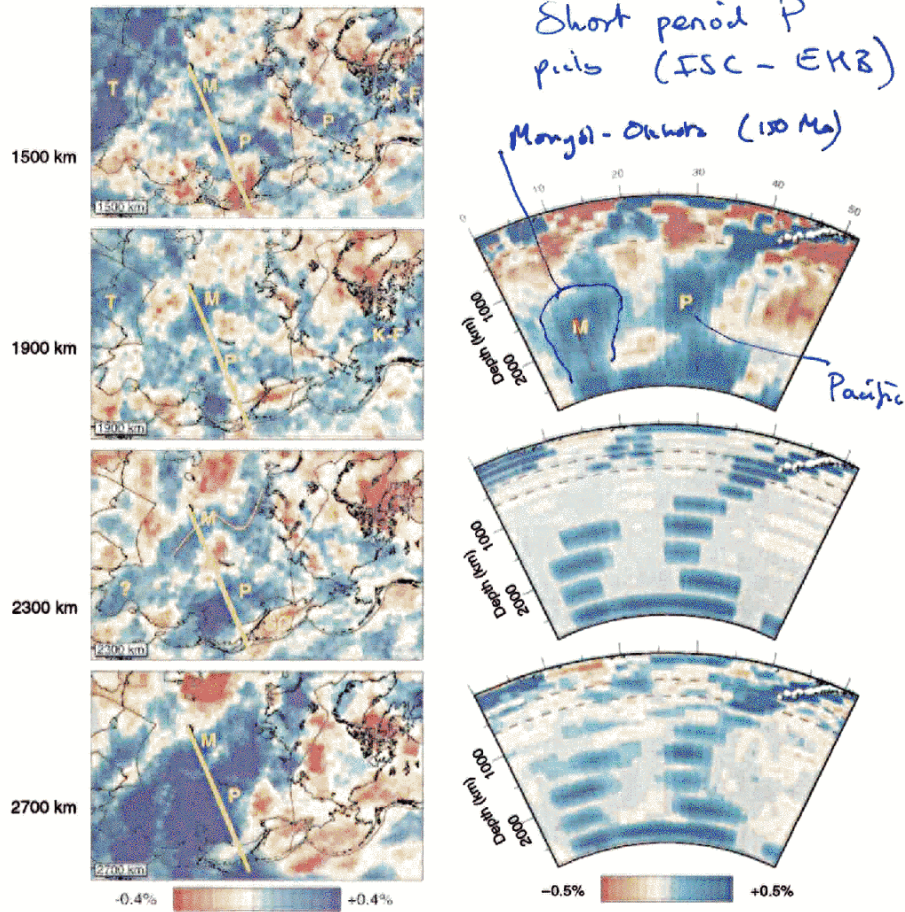
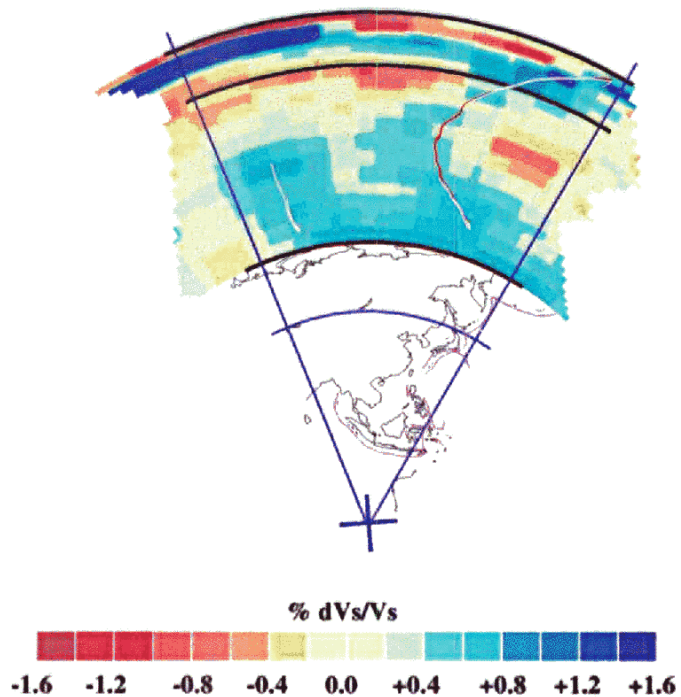


Figure 2 Tomographic P-wave velocity anomaly patterns in the deep mantle under Asia, for four different depths between 1500 and 2700 km. The superposed straight line indicates the location of the cross-section of Fig. 3. Velocity anomalies are displayed in percentages with respect to the average P-wave velocity at depth from model at 136°. Capital letters represent our interpretation of the Mongol-Okhotsk (M), Pacific (P), Tethyan (T) and Kula-Farallon (K-F) oceanic lithospheric slabs in all four frames; lower-case letters in the 2300 km frame represent geographical features: b, Lake Baikal; so, Sea of Okhotsk; v, Verkhoyansk suture; x, present-day North Pole. The question mark denotes a 'slab' of uncertain origin.

Figure 3 Cross-section through tomographic model. Top, tomographic results displayed in a vertical section along the line indicated in Fig. 2, showing the Pacific (P) subduction zone under Japan (right) and the inferred Mongol-Okhotsk slab (M) discussed here (left) side-by-side. White dots show locations of earthquakes in the west Pacific-Berloff zone. Middle, a simulated input of a whole-mantle layer-cake model¹⁸ for this same cross-section, which is resolved and (partially to completely) reproduced in our inversion analysis (bottom).

SB4L18



"Long-period" S model

Resolution and error

Let A^+ be an estimate of the inverse of A and let E be the covariance matrix of the data (usually taken to be diagonal and unity after error scaling)

- Resolution:

$$y = A \cdot x \quad \hat{x} = A^+ \cdot y$$

$$\hat{x} = A^+ A \cdot x$$

For an SVD inversion where $A^+ = V \cdot \Lambda^{-1} \cdot U^T$

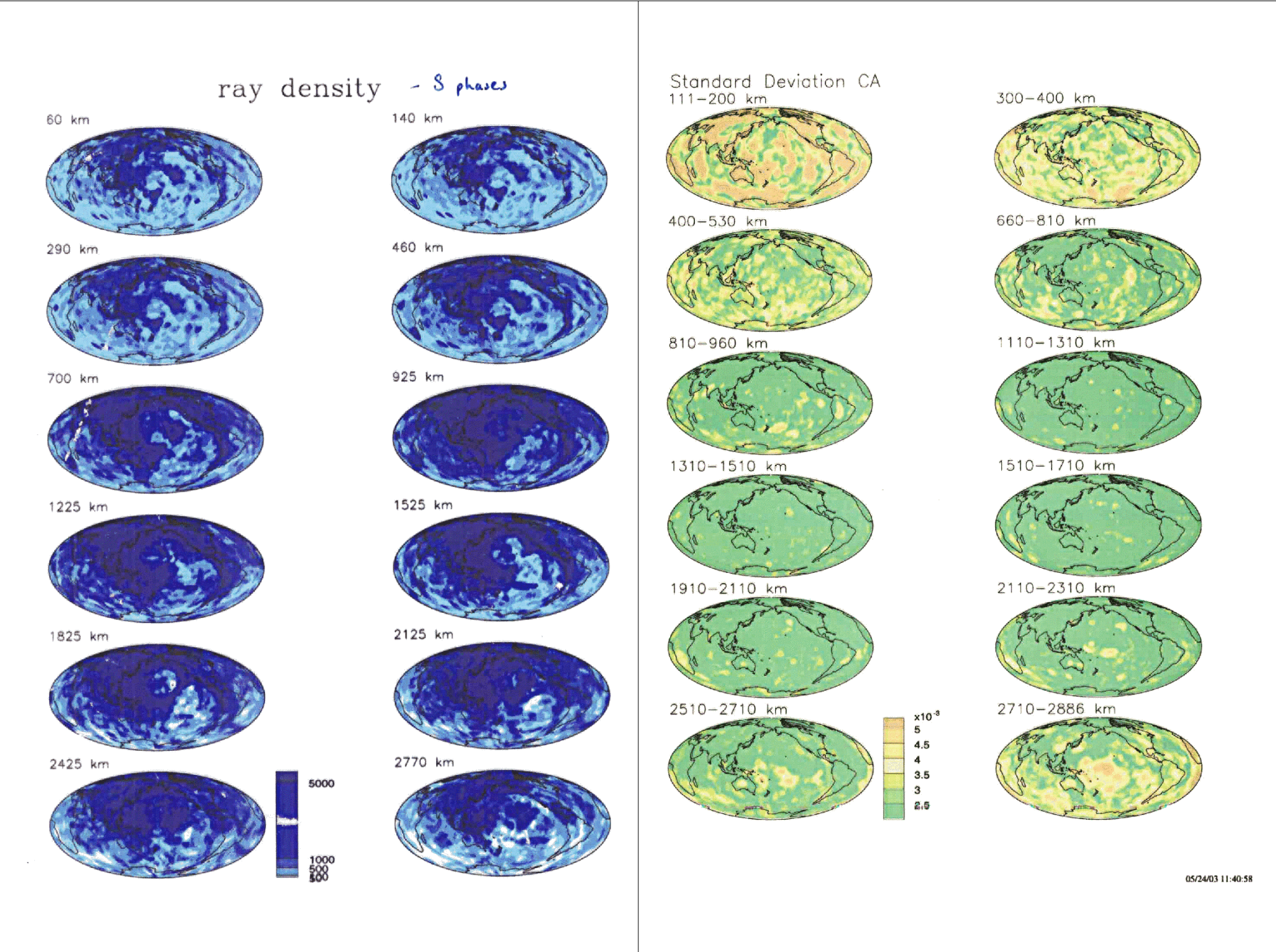
$$A^+ A = V V^T$$

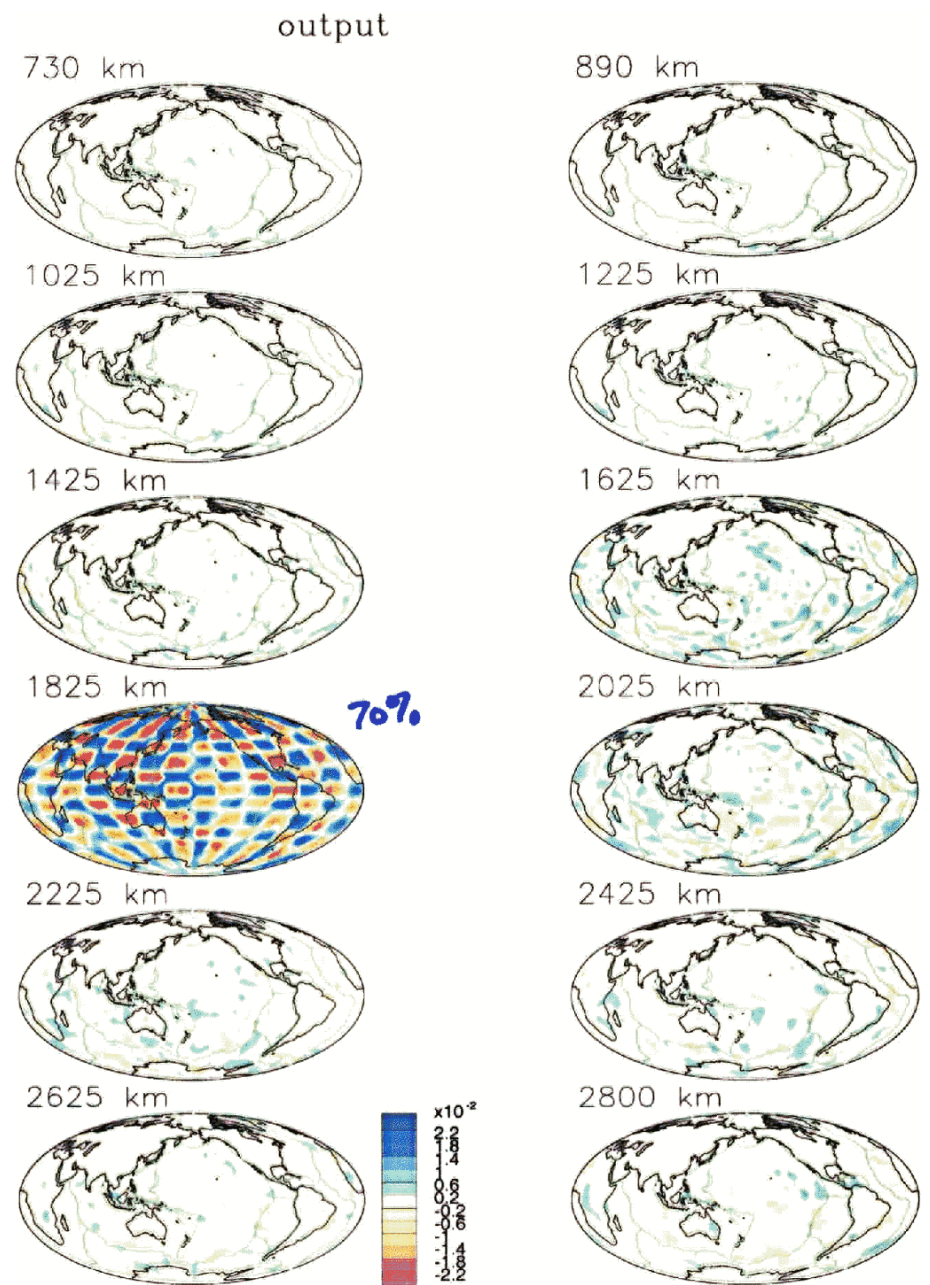
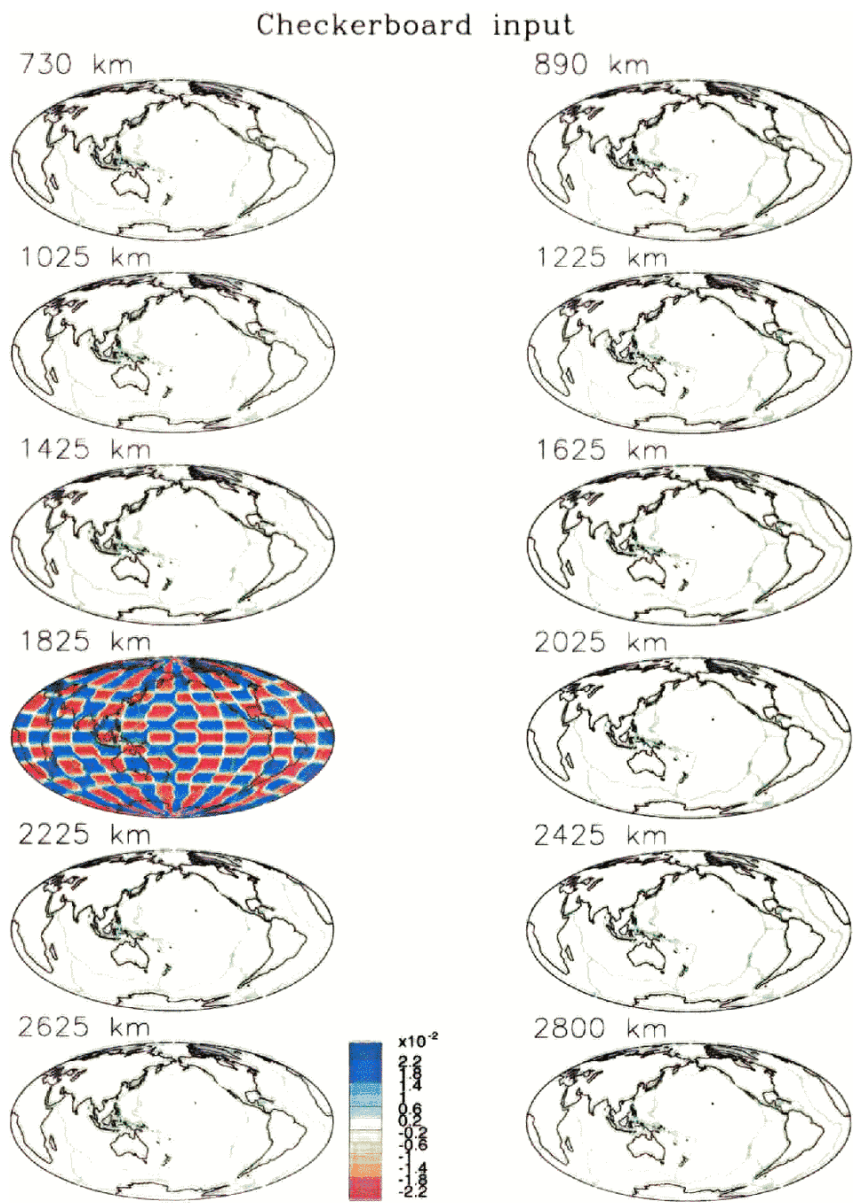
The model covariance matrix is given by

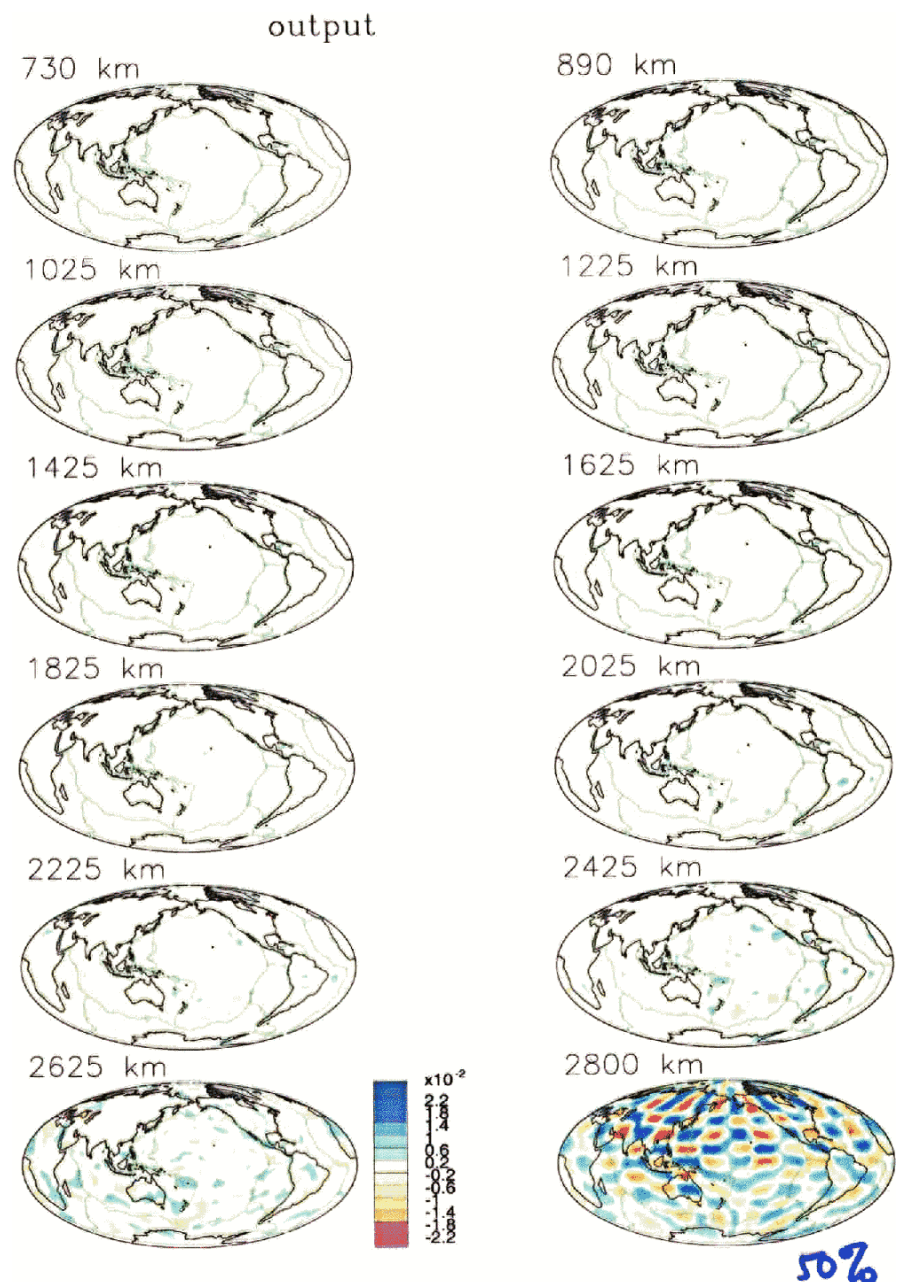
$$A^+ \cdot E \cdot A^{+T} = V \cdot \Lambda^{-2} \cdot V^T$$

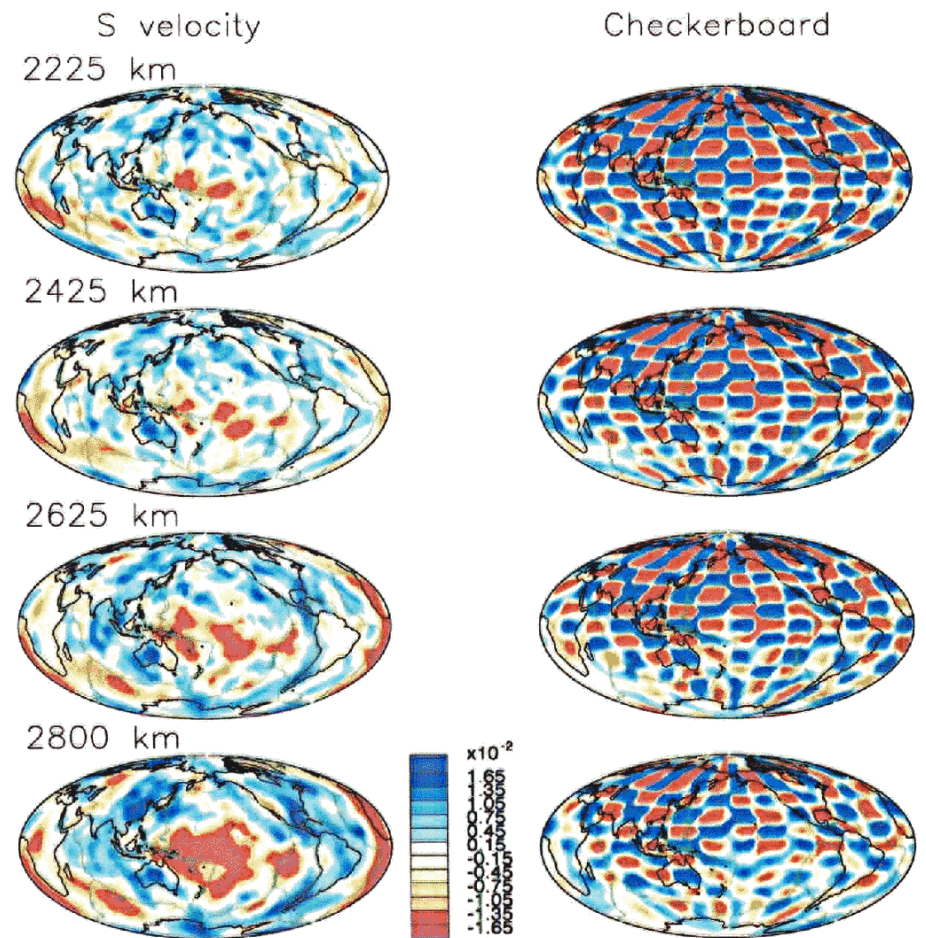
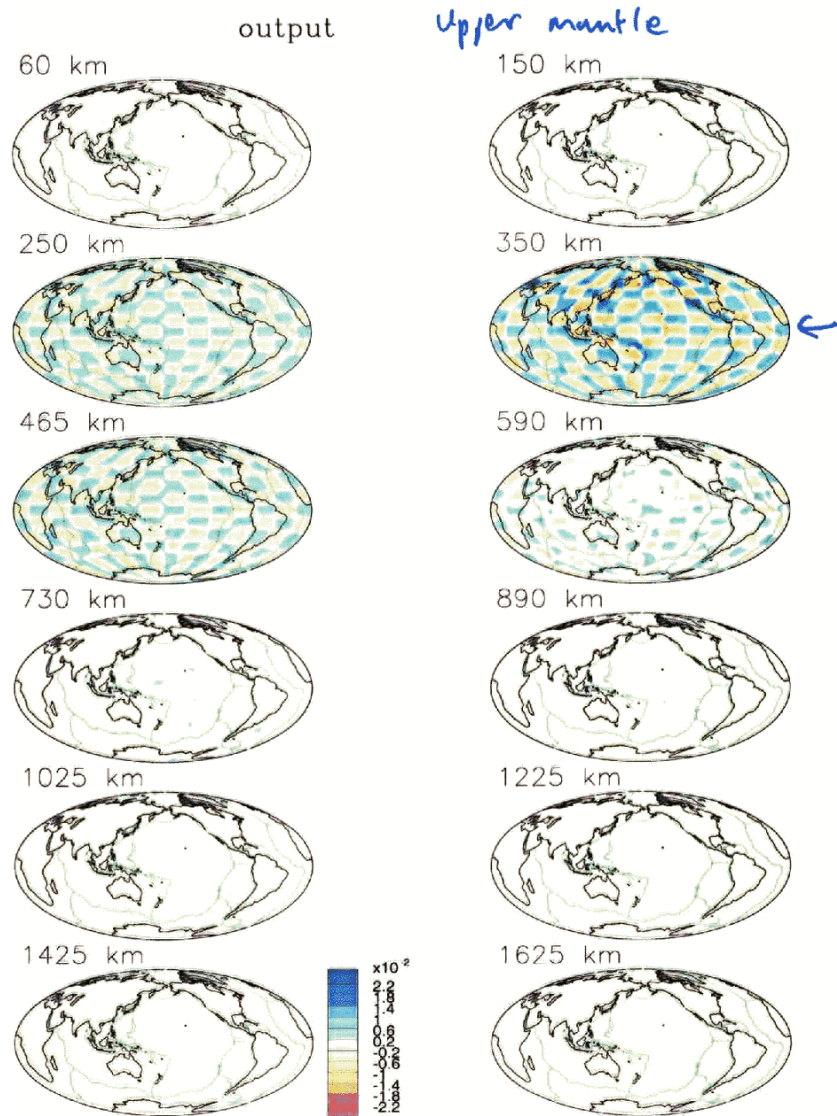
Solutions:

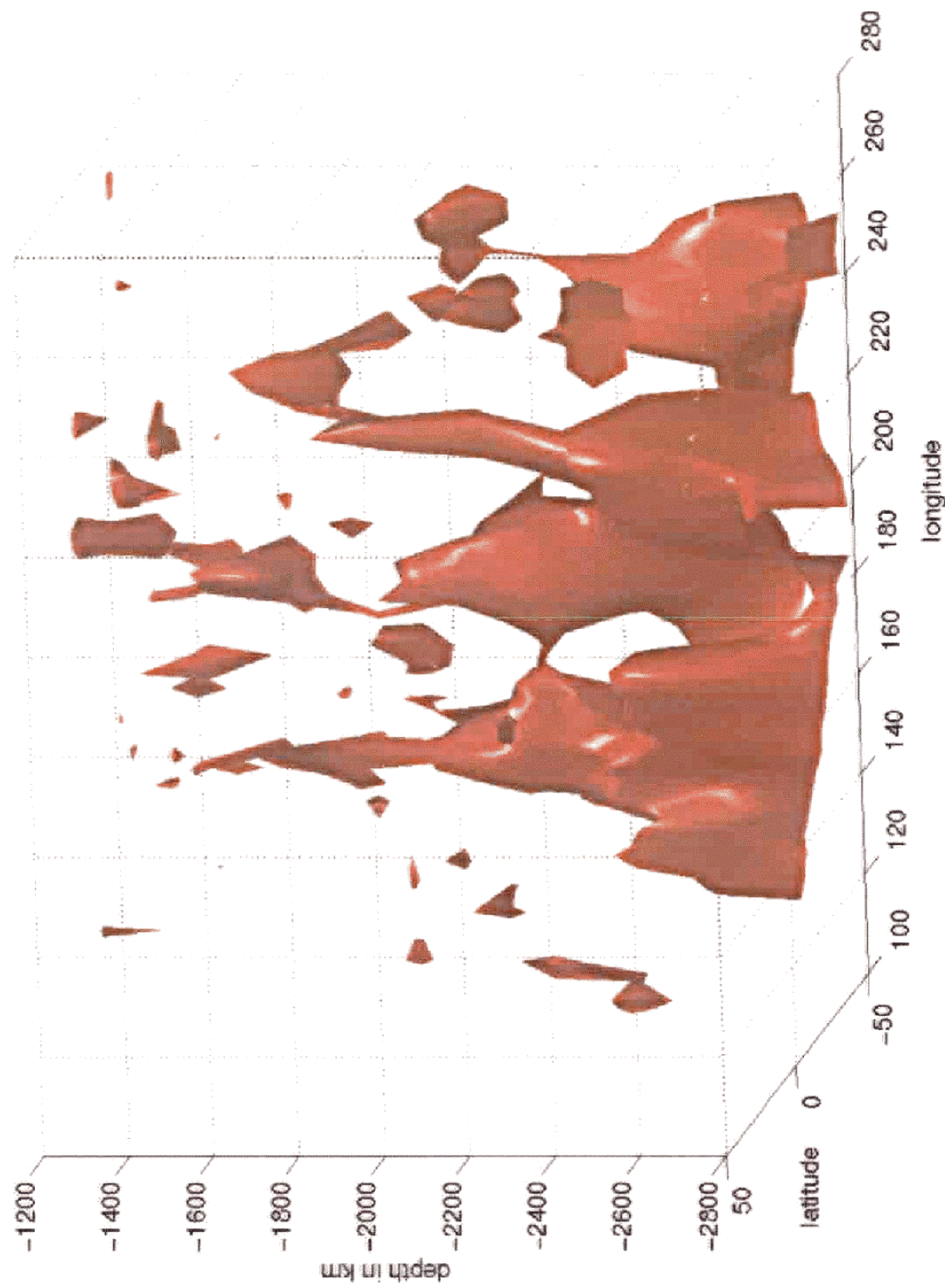
- Estimate A^+ using a backprojection
- Compute selected singular values and singular vectors using SVDPACK for sparse matrices
- Compute a row of the resolution matrix by doing a spike test
- Do a checkerboard test
- Estimate errors using a monte-carlo technique











Bulk Sound Speed, V_c

Bulk Modulus $\kappa_s = \rho V_c^2 = \rho(V_p^2 - \frac{4}{3}V_s^2)$

Shear Modulus $\mu = \rho V_s^2$

$$\kappa_s + \frac{4}{3}\mu = \rho V_p^2$$

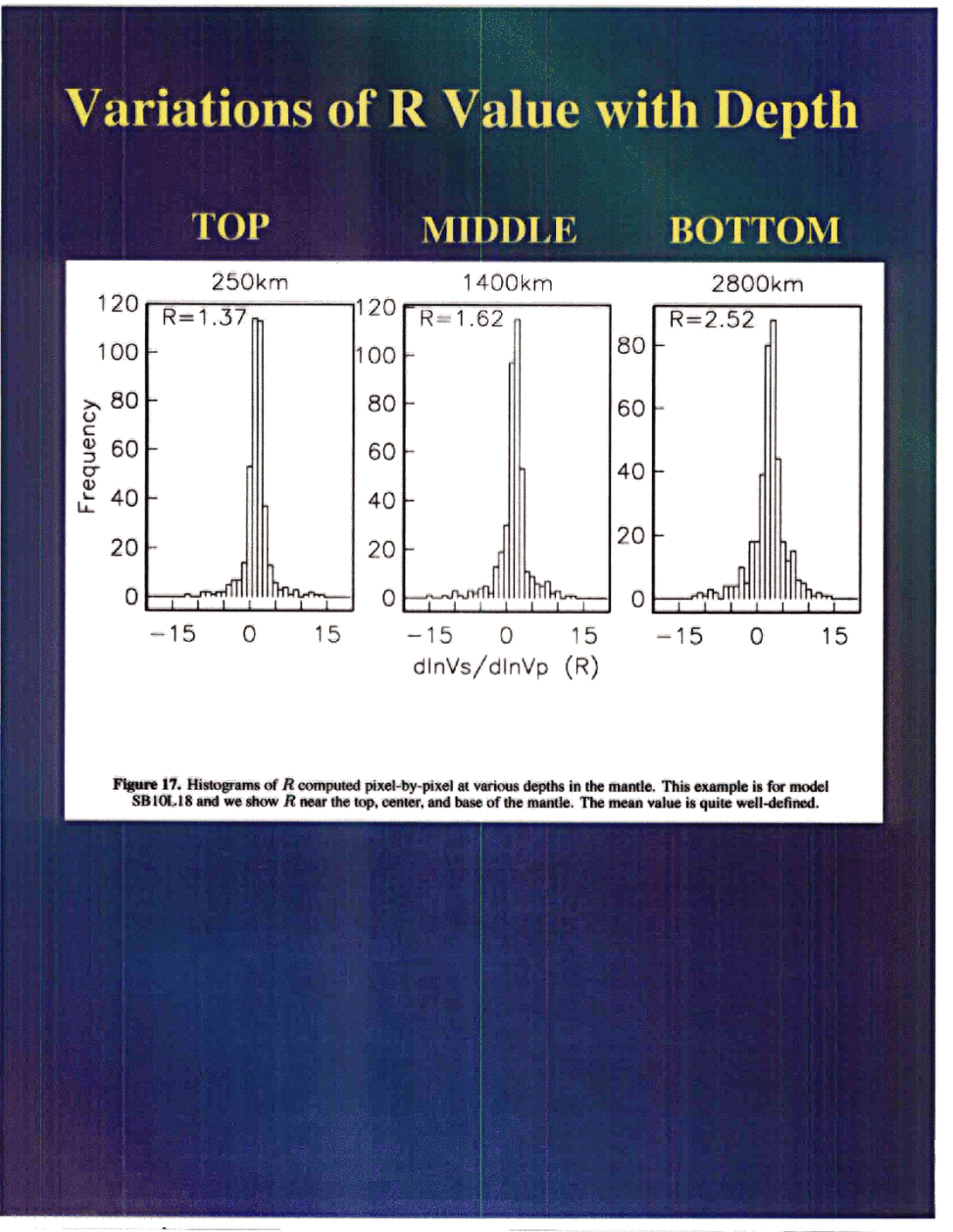
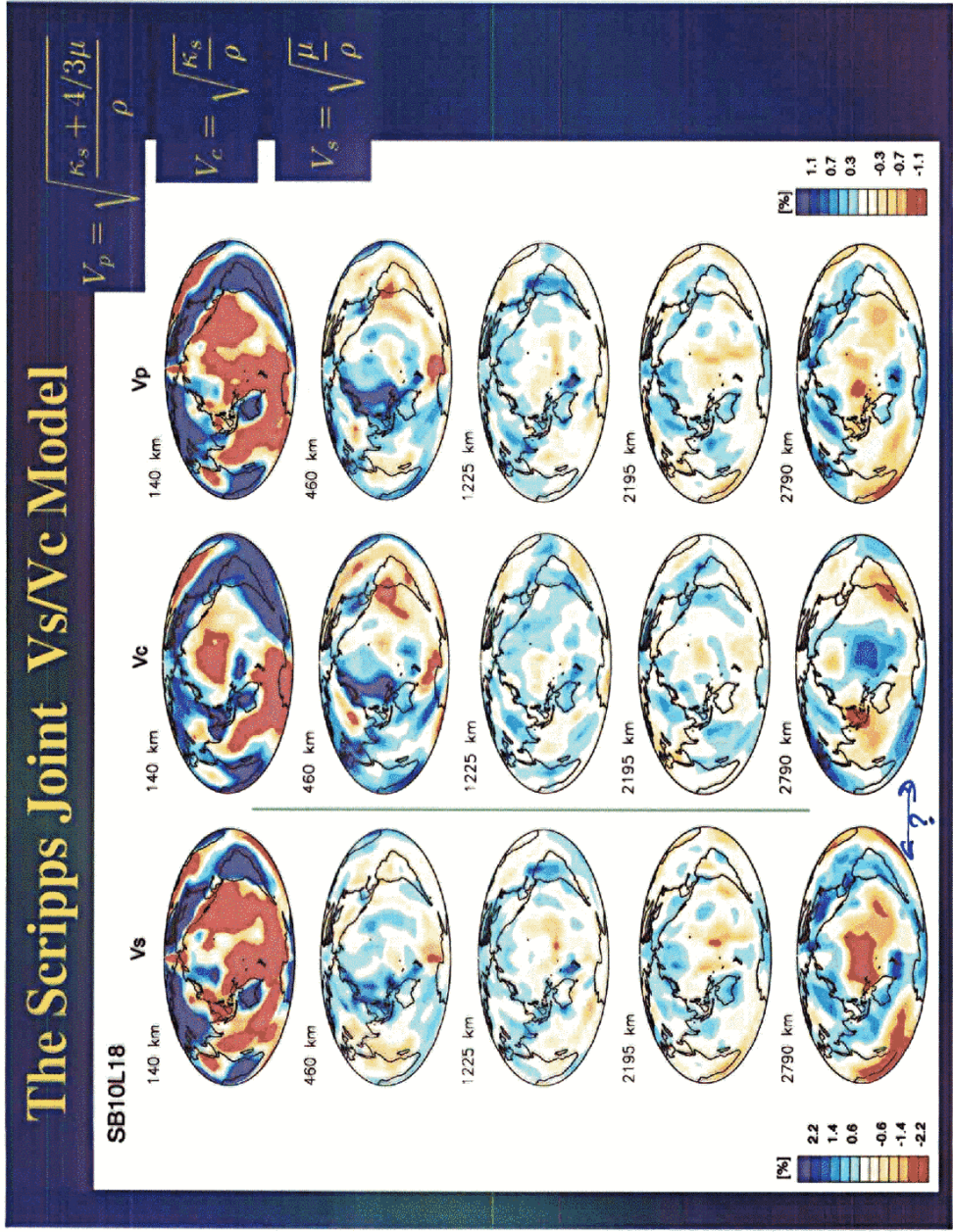
Shear Velocity $V_s = \sqrt{\frac{\mu}{\rho}}$

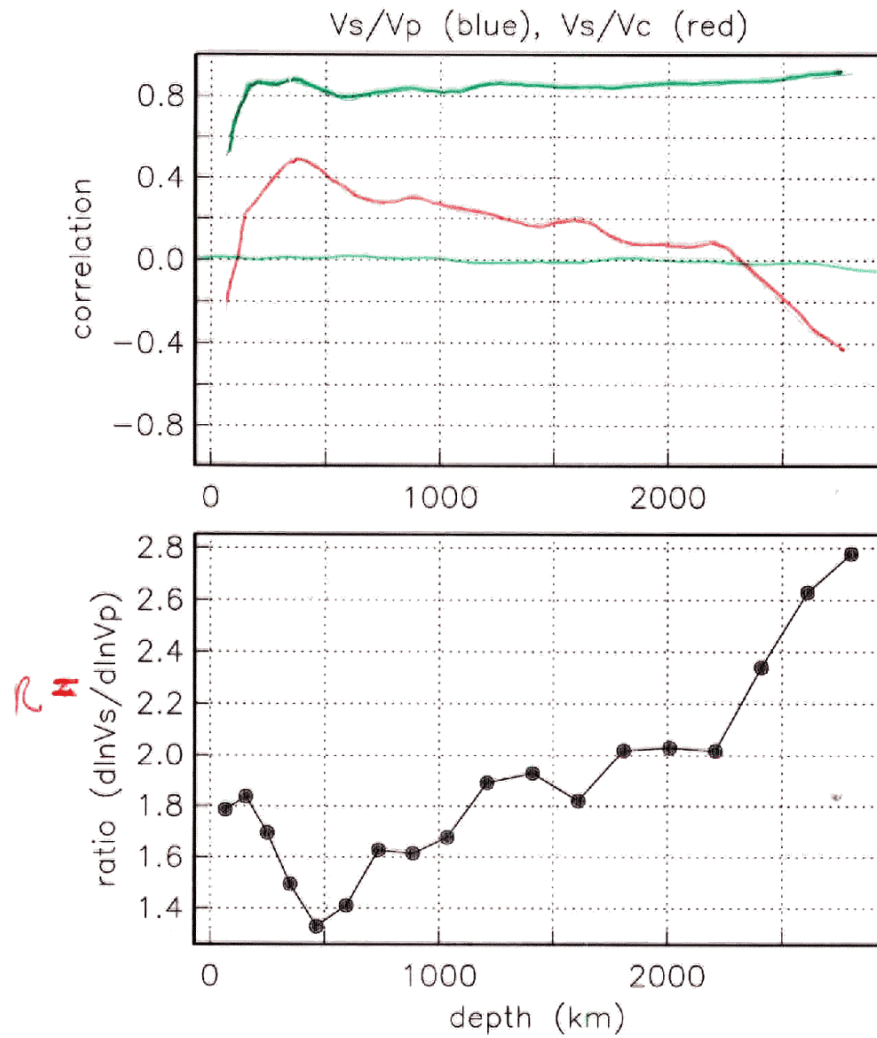
Bulk Sound Velocity $V_c = \sqrt{\frac{\kappa_s}{\rho}}$

Compressional Velocity $V_p = \sqrt{\frac{\kappa_s + 4/3\mu}{\rho}}$

Anomalies $\frac{\delta V_p}{V_p} = (1 - x) \frac{\delta V_c}{V_c} + x \frac{\delta V_s}{V_s}$

$$x = \frac{4}{3} \frac{V_s^2}{V_p^2} \simeq 0.4$$





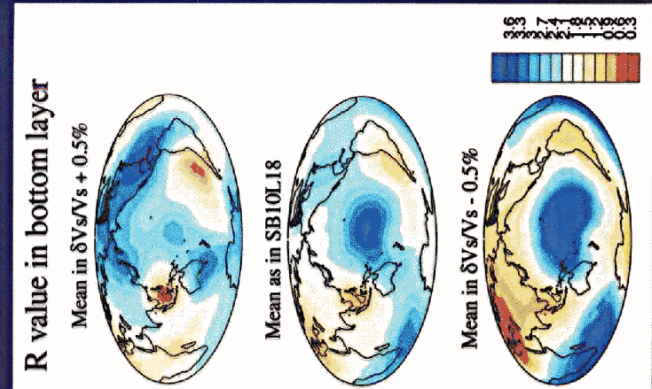
Anharmonic
 + anelastic

Thermal $\Rightarrow R \approx 1.3$
 Thermal $\Rightarrow R \approx 1.8 \rightarrow 2.0$

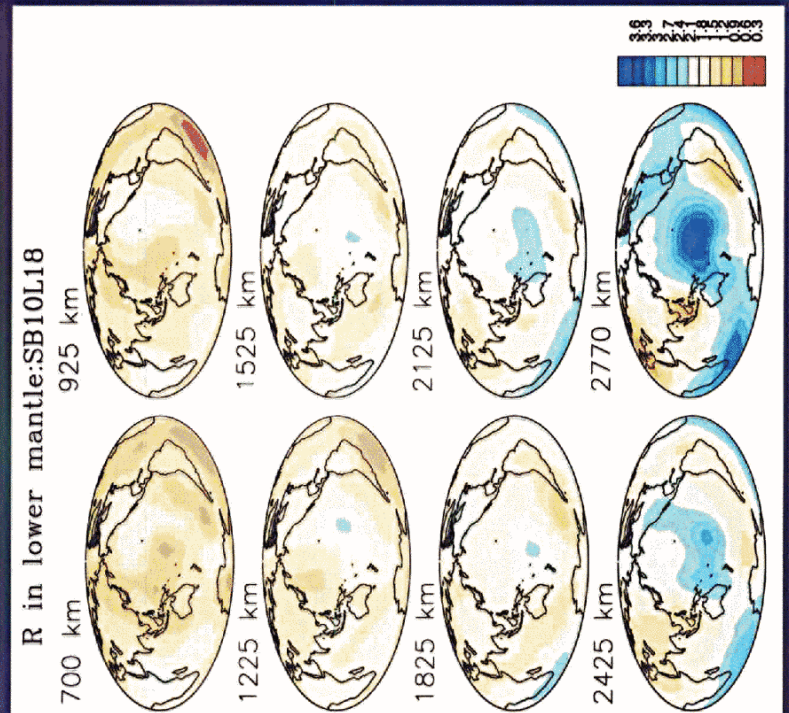
The R Value in the Lower Mantle

$$R = \frac{\delta V_s / V_s}{\delta V_p / V_p}$$

Trade-Off between R and
Mean of $\delta V_s / V_s$



R from inversion for SB10L18



SALTZER ET AL: P AND S WAVE HETEROGENEITY IN THE MANTLE 1337

that through much of the mantle there is no significant correlation between the bulk-sound and S-wave perturbations, although the magnitude and slope of the correlation coefficients as a function of depth is similar to that of Masters et al. [2000]. It is possible that this lack of correlation is due to compositional heterogeneity throughout the lower mantle or that the contribution of the bulk modulus is small. It is also possible that our bulk-sound wavespeed model is too noisy for this comparison.

Next, we distinguish regions where there has been subduction in the last 120 million years from those where there has not and loosely divide the mantle into four depth intervals: I (0-660 km), II (660-1500 km), III (1500-2400 km), and IV (2400-CMB). In the upper mantle (depth I), which is best sampled beneath earthquakes and stations, and the mid-mantle (depth II), which is generally well sampled, we find no significant differences in $\partial \ln V_s / \partial \ln V_p$ between regions where there has and has not been subduction in the last 120 million years (Figure 3a). However, in the lower mantle the curves have different slopes and begin to diverge at ~1000 km depth. The lack of a statistically significant difference between the slab and non-slab regions to at least 1200 km depth is consistent with an interpretation that the anomalies have a thermal origin.

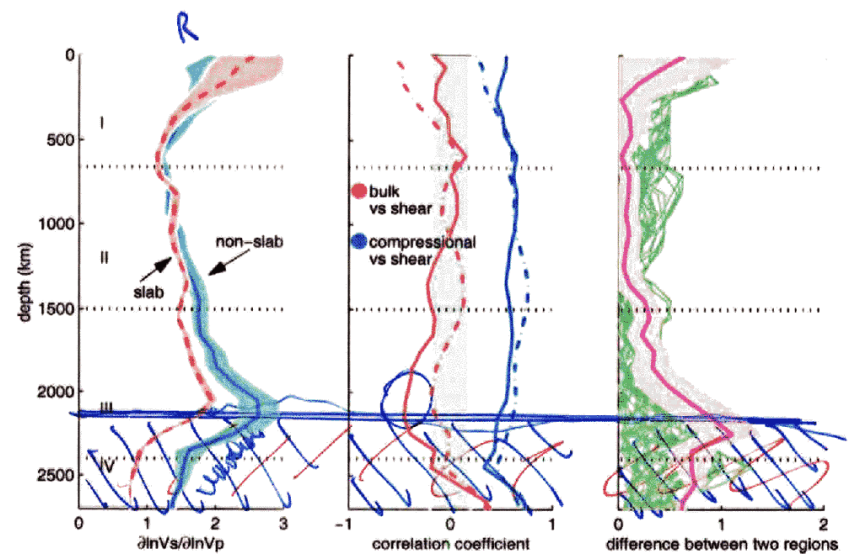


Figure 3. (a) S-wave versus P-wave model perturbations in non-slab regions (solid line) versus slab regions (dashed line) as a function of depth. The shaded areas indicate the 1σ uncertainty and encompass the models allowed by the data. (b) Correlation coefficients for bulk and shear (pair on the left) and P and S-waves (pair on the right) as a function of depth. Slab regions shown with dashed and non-slab regions with solid lines. The gray zone around zero depicts the range within which the correlations are not thought to be significant. Throughout most of the mantle the bulk and shear models are not significantly correlated except for a negative correlation between 1700 and 2400 km depth. The P and S-wave models are positively correlated throughout the mantle. (c) Difference between the slab and non-slab regions for a series of regionalizations shifted by 10 degree intervals around the globe (green). The regionalization shown in Figure 1 is the one that produces the largest difference between the slab and non-slab regions (pink curve) in the lower mantle, demonstrating that the differences are not due to a bias in sampling or random chance.

unreliable in ISC joint P/S inversions

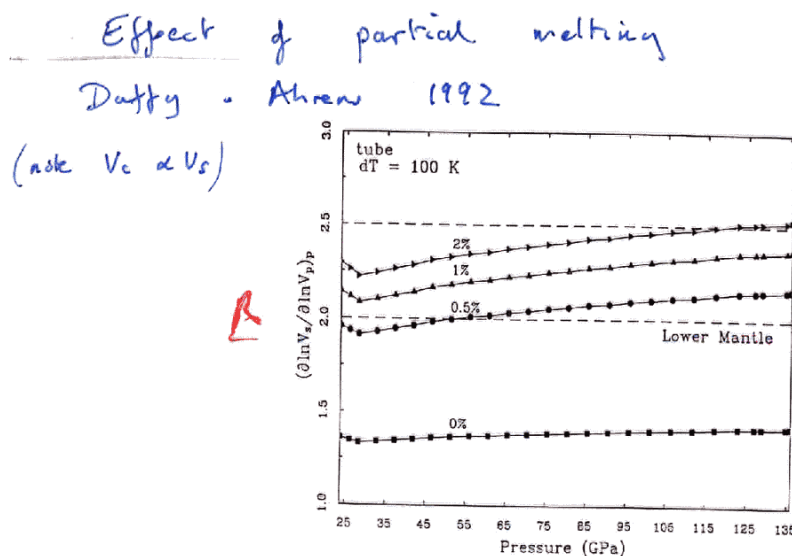


Figure 3. The parameter $(\partial \ln V_s / \partial \ln V_p)_p$ for melt fractions between 0 and 2% at lower mantle pressures. The case shown is for melt distributed in tube-shaped bodies and with a thermal anomaly of 100 K. The bulk modulus of the melt is the same as the residual solid. Dashed lines represent the range of lower mantle values from tomography.

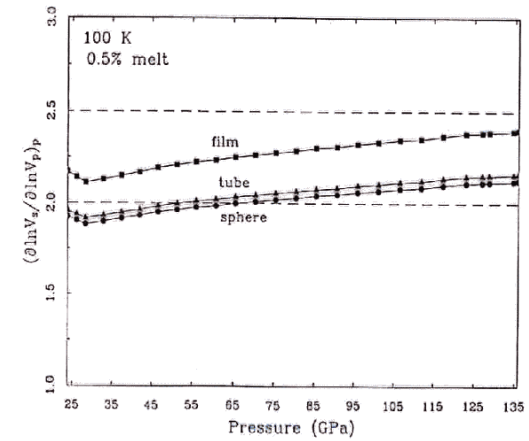
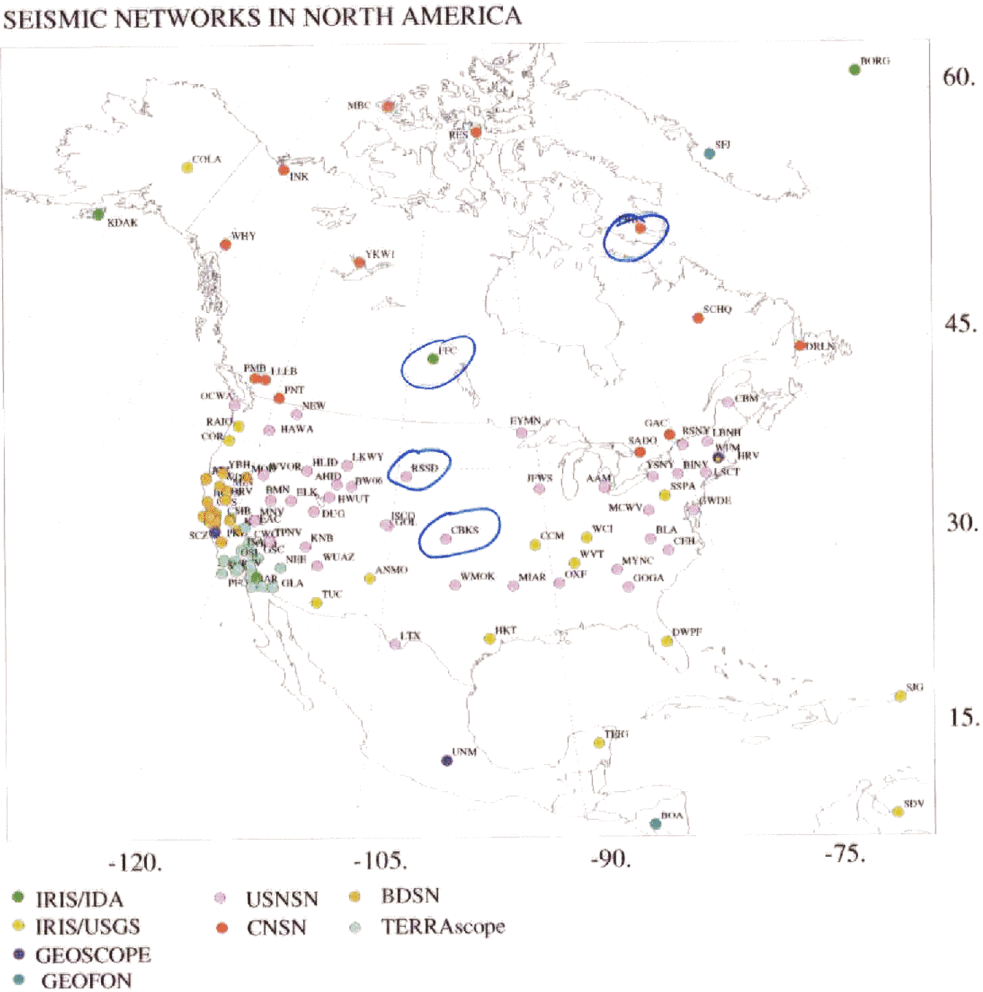
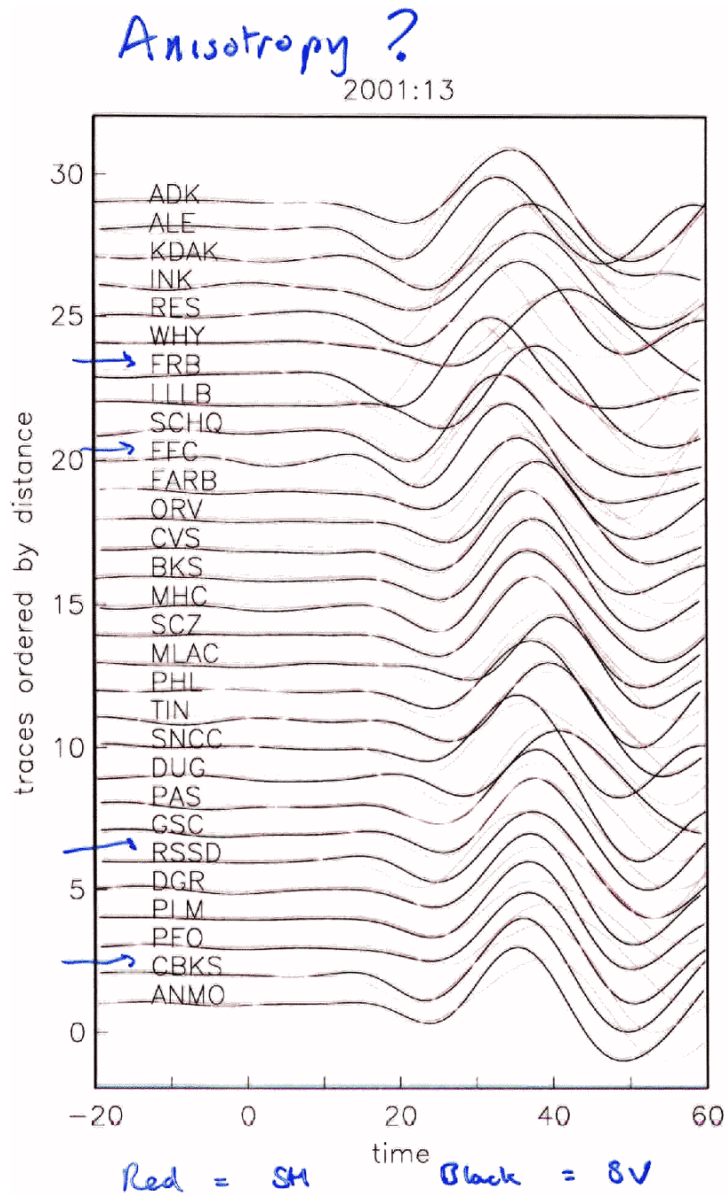


Figure 4. The parameter $(\partial \ln V_s / \partial \ln V_p)_p$ for different melt body geometries at lower mantle pressures. The thermal anomaly is 100 K and the melt fraction is 0.5%. In the case of the film, the aspect ratio is 0.05. Dashed lines represent the range of lower mantle values from tomography.





horizontal layering $\Rightarrow V_{sh} > V_{sv}$

A simplified anisotropic inversion

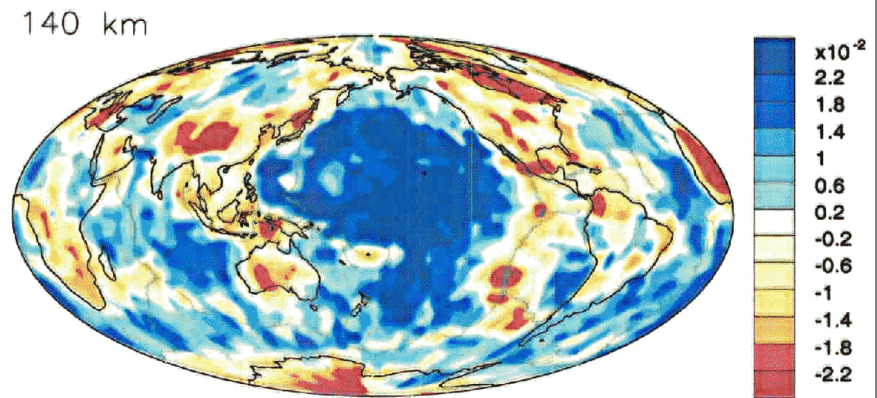
- Assume transversely isotropic: $V_{sv}, V_{sh}, V_{pv}, V_{ph}, \eta$
- Split times (when perturbing from an isotropic Earth) are given by:

$$\delta T_{SH-SV} = \int_{ray} \left[K_1 \left(\frac{\delta V_{sh}}{V_{sh}} - \frac{\delta V_{sv}}{V_{sv}} \right) + K_2 \left(\frac{\delta V_{ph}}{V_{ph}} - \frac{\delta V_{pv}}{V_{pv}} \right) + K_3 \frac{\delta \eta}{\eta} \right] d\Gamma$$

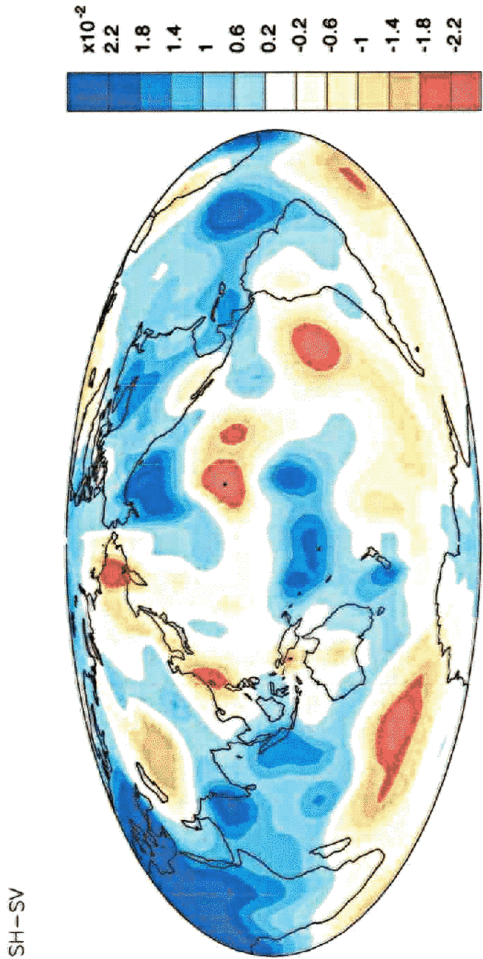
- Assume some scalings: anisotropy in S similar to anisotropy in P
- SH times ($S, SS - S, ScS - S$) are given by

$$\delta T = \int_{ray} \left[K_4 \frac{\delta V_{sh}}{V_{sh}} + K_5 \frac{\delta V_{sv}}{V_{sv}} \right] d\Gamma$$

SH-SV BOSCHI + EKSTRÖM 2003



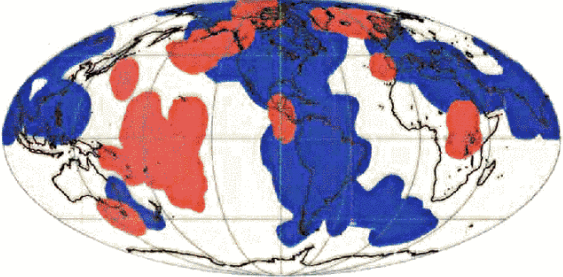
Anomalous Pacific



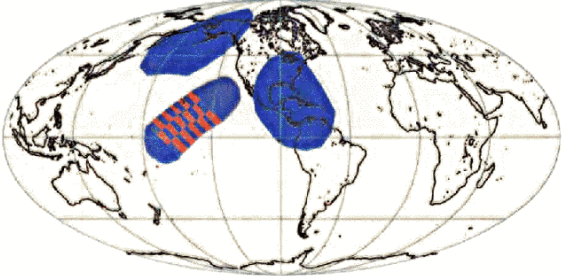
The core - mantle boundary layer and deep Earth dynamics

Thorne Lay, Quentin Williams & Edward J. Garnero

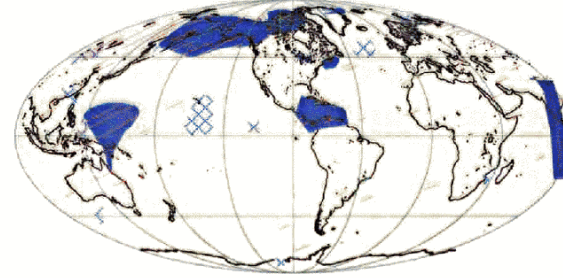
a ULVZ: red - observed, blue - not observed



b D" anisotropy: red - SV>SH, blue - SH>SV



c D" shear discontinuity: blue - observed, red - not observed



REPORTS

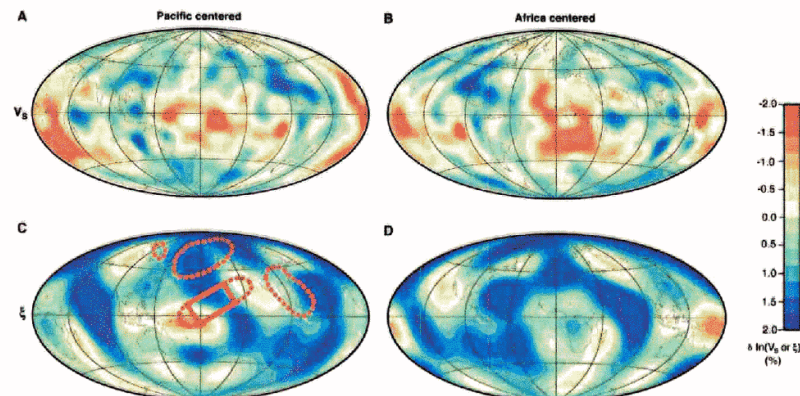


Fig. 2. Distribution of $\delta \ln(V_s)$ (A and B) and $\delta \ln(\xi)$ (C and D) at a depth of 2800 km. Maps are shown centered under the Pacific (A and C) and Africa (B and D). Also shown in C are the regions of D'' sampled by previous regional studies. Dotted areas indicate observations of $V_{SH} > V_{SV}$; the box in the central Pacific denotes a region with highly variable

upper mantle, as indicating the presence of strong horizontal shear, consistent with previous work (14–17). The isotropic part of the model (Fig. 2, A and B) is consistent with earlier tomographic models of shear velocity in this depth range (10, 18, 19) and is characterized by a strong degree 2 component representing a fast ring surrounding two low-velocity features (often called superplumes) centered beneath the central Pacific Ocean and Africa. The strong degree 0 component in ξ [$\delta \ln(\xi) > 0$] dominates the map in D'' (Fig. 2, C and D). The regions that differ most strongly from this average structure correlate well with the locations of the two superplumes, with reduced values of $\delta \ln(\xi)$ under the central Pacific Ocean, Africa, and the south Atlantic Ocean, including patches with negative values ($V_{SH} > V_{SV}$). Another two large patches of reduced $\delta \ln(\xi)$ are seen just west of North America and under central Eurasia. These patches also are related to slow isotropic velocities, although these regions of depressed velocities are much smaller than the two superplumes.

Although the finer scale features of our model may not be resolvable, and although observations in regions with high gradients will display some differences due to the long-wavelength parameterization of our model (20), the long-wavelength anisotropic features imaged in our model generally agree with more localized studies of D''

anisotropy (Fig. 2C). Specifically, earlier studies imaged areas with positive $\delta \ln(\xi)$ beneath Central America and Alaska (5, 8) as well as northeastern Asia (7). The central Pacific regional results are more variable, with some areas showing negative $\delta \ln(\xi)$ (3, 5, 8).

The dominant $V_{SH} > V_{SV}$ found as one approaches the CMB suggests that the anisotropy observed in D'' is related to the dominant horizontal flow in a mechanical boundary layer, analogous to the larger signal observed in the uppermost 200 km of the mantle and factored into the construction of the Preliminary Reference Earth Model (PREM) (17). As one approaches regions of upwelling, the direction of flow changes and results in a different signature of anisotropy, as manifested in our study under the central Pacific and Africa. Anisotropy in these regions bordering the large-scale upwellings may be much more complex and include tilting of the axis of symmetry, which we assume to be vertical in our modeling. This would result in azimuthal anisotropy, which we do not attempt to model here.

Whether the globally observed anisotropy is due to lattice-preferred orientation (LPO) (2, 21) or the alignment of materials with differing elastic properties through shape-preferred orientation (SPO) (3) must await direct measurements of how lowermost mantle materials will develop

LPO anisotropy at the corresponding temperature and pressure conditions. Arguments for weak anisotropy in perovskite [(Mg,Fe)SiO₃] and strong positive ξ in periclase (MgO) (2) as well as for negative ξ in both perovskite and periclase (22) have been advanced with the use of theoretical methods. Some studies have shown that high strain in subducting slabs approaching the CMB might be able to sustain conditions necessary for producing LPO structure across broad regions of D'' (21). This model also shows that although the major axes of the strain ellipses are horizontal under the downgoing slabs, the material can be rotated to vertical as it approaches upwellings, possibly explaining the observed change in anisotropy below the superplumes in our model. Different SPO hypotheses have been advanced as well, mostly relating to horizontal layering or inclusion of variously shaped pockets of contrasting material. Candidates for the differing elastic properties include reaction products from core-mantle interaction (23) and melted former basalt in a slab graveyard (3, 5). In general, these SPO models lead to positive ξ , although if there is tilting of the pockets of differing material under deformation, considerable azimuthal variation in velocities could be observed (2).

Whatever the cause, our results clearly show that the dynamics of D'' correspond with what would be expected in a boundary

Some geophysical conclusions

- Most anomalies in the lower mantle can be explained by "normal" subsolidus thermal effects
- Slow regions in the lowermost mantle are not "normal". Probably not ^{only} partial melting (since bulk sound speed perturbations are negatively correlated with shear velocity perturbations).
- Signal can't be explained by anisotropic effects alone
- Need chemical changes – or a phase change which can occur in the hotter slow regions.
- Regions typically coincide with ULVZs

Future directions

Tomography:

- Ocean bottom stations
- Improved theory and waveform modelling
- anisotropy and attenuation

frequency dependence
of travel times

Relation to other fields:

- “a priori” constraints on $V_p/V_s/\rho$ (MP)
- “a priori” constraints on nature of anisotropy (MP and GD)
- “a priori” constraints on discontinuities (MP)
- joint inversions with geodynamic data (GD)